

# Modelling iceberg capsizing in the open ocean

P. Bonnet<sup>1,2,3</sup>, V.A. Yastrebov<sup>3</sup>, P. Queutey<sup>4</sup>, A. Leroyer<sup>4</sup>, A. Mangeney<sup>2,5</sup>  
O. Castelnau<sup>2</sup>, A. Sergeant<sup>6</sup>, E. Stutzmann<sup>1</sup>, J-P Montagner<sup>1</sup>

<sup>1</sup>*Institut de Physique du Globe de Paris, Sorbonne Paris Cité, Seismology Group, CNRS UMR 7154, Paris, France*

<sup>2</sup>*Laboratoire Procédés et Ingénierie en Mécanique et Matériaux, CNRS, ENSAM, CNAM, Paris, France*

<sup>3</sup>*MINES ParisTech, PSL University, Centre des Matériaux, CNRS UMR 7633, Evry, France*

<sup>4</sup>*Laboratoire en Hydrodynamique Énergétique et Environnement Atmosphérique (LHEEA), METHRIC Team, CNRS UMR 6598, Centrale Nantes, France*

<sup>5</sup>*Université Paris-Diderot 7, Sorbonne Paris Cité, UFR STEP, Paris, France*

<sup>6</sup>*Aix-Marseille Université, Centrale Marseille, Laboratoire de Mécanique et d'Acoustique, CNRS UMR 7031, Marseille, France*

## Summary

At near-grounded glacier termini, calving can lead to the capsizing of kilometer-scale (i.e. gigatons) unstable icebergs. The transient contact force applied by the capsizing iceberg on the glacier front generates seismic waves that propagate over teleseismic distances. The inversion of this seismic signal is of great interest to get insight into actual and past capsizing dynamics. However, the iceberg size, which is of interest for geophysical and climatic studies, cannot be recovered from the seismic amplitude alone. This is because the capsizing is a complex process involving interactions between the iceberg, the glacier and the surrounding water. For this reason, we propose an approach based on the computation of the source force with a mechanical model for various iceberg geometries and the estimation of the iceberg size from a comparison of the computed and seismically inverted time histories of the force. The capsizing dynamics is captured by computational fluid dynamic (CFD) simulations for a simple scenario of capsizing in the open ocean without glacier front. This approach allows assessing the complexity of the fluid motion around an iceberg and how far the ocean is affected by iceberg rotation. Expressing the results in terms of appropriate dimensionless variables, we show that laboratory scale and field scale capsizes can be directly compared. The capsizing dynamics is found to be highly sensitive to the iceberg aspect ratio and to the fluid and ice densities. However, dealing at the same time with the contact between the iceberg and the deformable glacier front requires highly complex coupling that often goes beyond capabilities of fluid-structure interaction softwares. Therefore, we present a semi-analytical simplified fluid-structure model (SAFIM) that can be implemented in solid mechanics models dealing with contact dynamics. This model accounts for hydrodynamic forces through calibrated drag and added-mass effects. We show that SAFIM significantly improves the accuracy of the modeled horizontal force and horizontal iceberg velocity compared with previously published simplified models. SAFIM has been calibrated against the reference CFD simulations. Various types of drag forces are discussed. The one that provides the best results is an integrated pressure force proportional to the square of the normal local velocity at the iceberg's surface, with a drag coefficient depending linearly on the iceberg aspect ratio. A new formulation of simplified added-masses and a computed added-mass proposed in the literature, are also discussed. The former formulation, when combined with an empirical drag model, provides a better match with the reference results than the latter. The drag force mainly affects the amplitude of the fluid forces and this amplitude is best predicted without added-masses. The error on the modeled horizontal force ranges between 5% and 25% for different aspect ratios. The added-masses affect the initiation period of the capsizing, the duration of the whole capsizing being better simulated when added-masses are accounted for.

**Keywords:** Numerical modelling, Glaciology, Sea level change, Fracture and flow, Theoretical seismology, Earthquake dynamics

# 1 Introduction

A current concern in climate science is the estimation of the mass balances of glaciers and ice sheets. The Greenland ice sheet mass balance contributes significantly to sea level rise, accounting for about 15% of the annual global sea level rise between 2003 and 2007 [Jay Zwally et al., 2011]. However, it is difficult to draw conclusions on general trends given the high uncertainties [Lemke et al., 2007] in these estimations, notably due to difficulties in estimating and partitioning the ice-sheet mass losses [van den Broeke et al., 2009]. Ice mass balance can be determined by calculating the difference between the (i) surface mass balance, mainly determined by inland ice gains minus ice losses and (ii) dynamic ice discharge, mainly made up of submarine melting and iceberg calving [Van Den Broeke et al., 2016]. One third to one half of the ice mass losses of the Greenland ice sheet are due to dynamic ice discharge [Enderlin et al., 2014]. Note that dynamic ice discharge is a complex phenomenon, influenced by ocean and atmospheric forcing and by glacier geometry and dynamics [Benn et al., 2017].

When a glacier marine terminus approaches a near-grounded position, calving typically occurs through the capsizing of glacier-thickness icebergs. An iceberg will capsizes under buoyancy for a width-to-height ratio below a critical value [MacAyeal and Scambos, 2003]. In Greenland, buoyancy-driven iceberg capsizing can cause a horizontal and vertical movement of the glacier tongue [Murray et al., 2015], potentially destabilizing or restabilizing the ice tongue depending on variations of the glacier's flotation state [Cassotto et al., 2019]. Iceberg capsizing can also trigger ice-shelf break-off as observed in Antarctica [MacAyeal and Scambos, 2003, Burton et al., 2013]. Capsizing icebergs can slowly push ice-mélange away from the glacier front [Amundson et al., 2010] or squeeze it and rigidify it [Peters et al., 2014], which can affect the stabilizing buttressing stresses produced by ice-mélange at the calving front [Todd and Christoffersen, 2014]. Note that during capsizing, important volumes of fjord water are mixed [Burton et al., 2012], which can affect fish populations [Moon et al., 2016]. Moreover, icebergs deteriorate through various processes such as break-up, wave erosion and solar or submarine convection melting [Job, 1978, Savage, 2007], which releases freshwater that can potentially affect overturning ocean circulation [Vizcaino et al., 2015, Marsh et al., 2015]. [Wagner et al., 2017] explain that icebergs mainly melt through wind-driven wave erosion that leads to lateral thinning and thus eventually a buoyancy driven capsizing of the iceberg (width-to-height ratio below a critical value [MacAyeal and Scambos, 2003]). Moreover, iceberg drift model simulations have shown that capsizing icebergs live longer and drift further than non-capsizing icebergs [Wagner et al., 2017].

When they capsizes right after calving, icebergs exert an almost horizontal transient contact force on the glacier front. This force is responsible for the generation of magnitude  $M_w = 5$  earthquakes that are recorded globally [Ekström Göran, 2003] and can be recovered from seismic waveform inversion [Walter et al., 2012, Sergeant et al., 2016]. Monitoring iceberg calving and capsizing with such "glacial earthquakes" is a promising alternative to satellite imagery or airborne optical and radar sensors that suffer from limited time and spatial coverage. There is no direct link between the size of an iceberg and the seismic signal [Tsai et al., 2008, Walter et al., 2012, Amundson et al., 2012, Sergeant et al., 2016, Sergeant et al., 2018] and many different processes involving the interactions between the iceberg, glacier, bedrock, water and ice mélange contribute to the type of calving, earthquake magnitude and seismic waveform [Amundson et al., 2010, Tsai et al., 2008, Amundson et al., 2012].

To investigate in detail the link between iceberg volume, contact force and the generated seismic signals, the use of a hydrodynamic model coupled with a dynamic solid mechanics model is mandatory. The iceberg-ocean interaction governs the iceberg capsizing dynamics and thus controls the time-evolution of the contact force which is responsible for the seismic waveform and amplitudes. Full modelling of the glacier-ocean-bedrock-iceberg-ice-mélange system is beyond capabilities of most existing models because it requires complex and costly coupling between solid mechanics, contact dynamics and fluid dynamics. The simplified models proposed in the literature to describe capsizing icebergs assume a 2D rectangular rigid iceberg under gravity and account for the buoyancy force, iceberg-glacier contact force and simplified hydrodynamic effects using either added-masses [Tsai et al., 2008] or pressure drag [Burton et al., 2012, Amundson et al., 2012, Sergeant et al., 2018, Sergeant et al., 2019]. These models have been proposed to describe a specific aspect of the capsizing: its vertical and rotational motion [Burton et al., 2012] validated against laboratory experiments, or the horizontal force that icebergs exert on the glacier fronts [Tsai et al., 2008, Sergeant et al., 2018]. To build a complete catalogue of seismogenic calving events that can be used for seismic inversion and iceberg characterization, the model must accurately describe the interaction between the iceberg and the ocean. At the same time, its formulation should either remain sufficiently simple

or be based on the interpolation on the response surface constructed on numerous full-model simulations. In particular, the horizontal force and the torque exerted by the fluid on the iceberg should be modelled as accurately as possible, since it controls the horizontal contact force [Tsai et al., 2008, Burton et al., 2012, Amundson et al., 2012, Sergeant et al., 2018].

The present paper aims to provide an understanding the complex interactions between a capsizing iceberg and the surrounding water using a reference fluid dynamics solver and to capture the main feature of this interaction in a simplified model formulation suitable for further computations of seismic wave sources. For this, we use a Computational Fluid Dynamics solver (ISIS-CFD Software for Numerical Simulations of Incompressible Turbulent Free-Surface Flows) to generate reference results for the capsizing motion. This model solves Reynolds Averaged Navier-Stokes equations (RANSE) and handles interactions between rigid solids and fluids with a free surface. This model is not yet able to compute dynamic contacts between solids. This state-of-art model has been largely validated for marine engineering cases [Visonneau, 2005, Queutey et al., 2014, Visonneau et al., 2016] but not yet applied to kilometre-size objects like capsizing icebergs in the open ocean, which give rise to high vorticity. Before applying ISIS-CFD to field-scale iceberg capsise, we will evaluate how well it can reproduce small-scale laboratory experiments (typical dimension of 10 cm). We will compare ISIS-CFD simulations to laboratory experiments conducted by [Burton et al., 2012] using a polymer proxy for icebergs capsizing in a narrow fjord-like water tank.

To obtain a model that can be easily coupled with a solid mechanics model, we will then propose a simplified formulation (SAFIM, for Semi-Analytical Floating Iceberg Model) for the interactions between iceberg and water. In this model, introduced hydrodynamic forces account for water drag and added-masses, these two effects being considered uncoupled and complementary. Such a complementary description of hydrodynamic forces was initially proposed for modelling the effect of waves on vertical piles [Morison et al., 1950] and has been widely used for modelling the effect of waves and currents on bulk structures [Venugopal et al., 2009, Tsukrov et al., 2002]. The SAFIM hydrodynamic forces involve some coefficients that need to be calibrated to represent the effects of the hydrodynamic flow on the capsise motion. To do so, SAFIM parameters are fitted against reference results provided by ISIS-CFD.

When an iceberg capsizes in contact with the glacier front, it exerts a force on the glacier until it starts to drift away which happens before the tilt angle reaches  $90^\circ$  [Amundson et al., 2012]. Therefore, in the goal of future investigation of seismic waves generated during the iceberg-to-glacier contact, we are mainly interested in the dynamics of a capsizing iceberg in the open ocean only until this value of the tilt angle - i.e.  $\theta < 90^\circ$ .

The paper is organized as follows. Section 2 presents the reference ISIS-CFD fluid dynamics model and its results are compared with those of laboratory experiments from [Burton et al., 2012]. The complexity of the fluid motion surrounding the iceberg and the pressure on the iceberg are then discussed. The similarities between the laboratory-scale and field-scale simulations are then presented. In section 3, we present the SAFIM simplified model and we discuss the assumptions with respect to those of other models from the literature. In Section 4, ISIS-CFD and SAFIM are compared for different case-studies and error quantification and fitting of parameters are discussed. Section 5 is an overall discussion: comparison of previous models, the new SAFIM model and the reference ISIS-CFD model, followed by a comparison of the results of drag and added-masses models compared with values computed by ISIS-CFD and discussion of the sensitivity of the model to geophysical variables such as the iceberg geometry and the density of water and ice.

## 2 Insights into iceberg capsise physical processes from computational fluid dynamics simulations

### 2.1 Considered geometry

In this paper, we investigate the capsise of unstable icebergs in the open ocean, i.e. away from the glacier front. Water and ice densities are noted  $\rho_w$  and  $\rho_i$ . For the field scale, we take the typical values of  $\rho_w = 1025 \text{ kg/m}^3$  and  $\rho_i = 917 \text{ kg/m}^3$ . For the laboratory experiments, the densities are set to  $\rho_w = 997 \text{ kg/m}^3$  and  $\rho_i = 920 \text{ kg/m}^3$  for direct comparison with [Burton et al., 2012]. The considered geometry is shown in Fig. 1. The upward vertical direction is denoted  $\mathbf{e}_z$  and the horizontal direction  $\mathbf{e}_x$ . The out-of-plane dimension  $L$  of the iceberg (i.e. along  $\mathbf{e}_y$ ) is assumed to be sufficiently large compared to the height  $H$  and the width  $W$  such that the problem can be considered as two-dimensional. This two-dimensional assumption is discussed in Section 5.6.

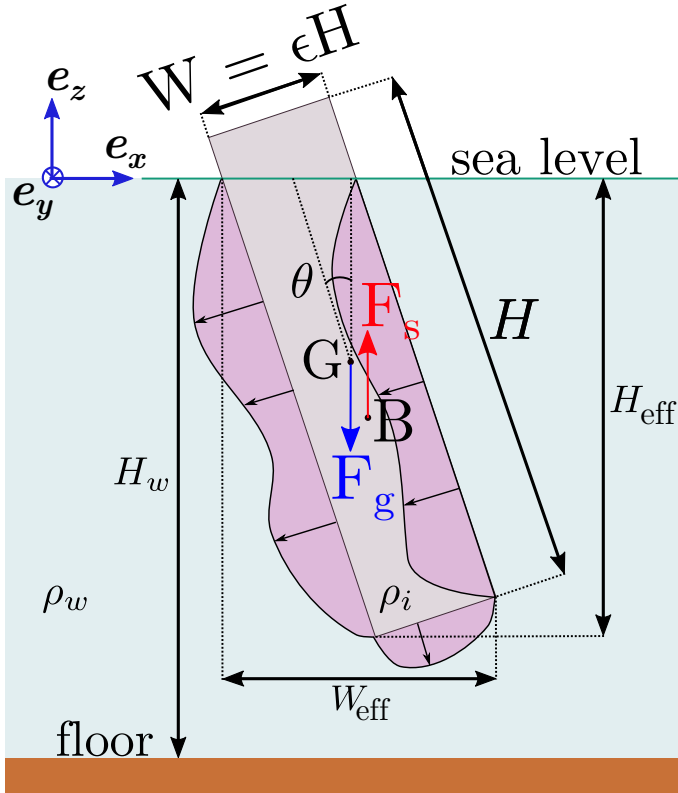


Figure 1: Iceberg geometrical characteristics with the iceberg centre of gravity  $G$  and the centre of buoyancy  $B$ . The forces acting on the moving iceberg are: the gravity force  $\mathbf{F}_g$ , the hydrostatic fluid force  $\mathbf{F}_s$  and the hydrodynamic pressure indicated by the pink shaded area.

In this two-dimensional set-up, icebergs are assumed to be rectangular with in-plane dimensions  $H$  and  $W$  and an aspect ratio defined as  $\varepsilon = W/H$ . Rectangular icebergs in a vertical position are unstable, *i.e.* will capsize spontaneously, for aspect ratios smaller than a critical value [MacAyeal and Scambos, 2003]:  $\varepsilon < \varepsilon_c = \sqrt{6 \rho_i \frac{\rho_w - \rho_i}{\rho_w^2}}$ . This critical aspect ratio is  $\varepsilon_c \approx 0.75$  for densities in the field and  $\varepsilon_c \approx 0.65$  for the densities in laboratory experiments. For  $\varepsilon > \varepsilon_c$ , icebergs are vertically stable and will not capsize unless initially tilted sufficiently [Burton et al., 2012].

The iceberg is assumed to be rigid, *i.e.* it does not deform elastically. The mass of an iceberg per unit of thickness along  $\mathbf{e}_y$  is given by  $m = \rho_i H^2 \varepsilon$ . Points  $G$  and  $B$  are the centre of gravity of the iceberg and the centre of buoyancy, respectively. The iceberg position is described by the horizontal and vertical positions of  $G$ , noted  $x_G$  and  $z_G$  respectively, and by the inclination  $\theta$  of the iceberg's longer side with respect to the vertical.  $H_w$  is the water depth.

## 2.2 Presentation of the ISIS-CFD solver

The ISIS-CFD solver, developed by LHEEA in Nantes (France), is a state-of-the-art solver for the dynamics of mixed turbulent flows [Guilmineau et al., 2017, Guilmineau et al., 2018] interacting with solid and flexible bodies [Hay et al., 2006, Leroyer and Visonneau, 2005, Durand et al., 2014] and with a free surface [Queutey and Visonneau, 2007, Leroyer et al., 2011]. Today, it is one of the very few available software products capable of solving problems as complex as interactions between solids and a fluid with a free surface. The target applications of ISIS-CFD are in the field of marine engineering, e.g. modelling the dynamic interactions between a ship and surface waves [Visonneau, 2005, Queutey et al., 2014, Visonneau et al., 2016] or the complex flows and interactions involved in the global hull-oars-rower system in Olympic rowing [Leroyer et al., 2012]. ISIS-CFD solves the Reynolds Averaged Navier-Stokes Equations (RANS) [Robert et al., 2019] and uses a few different turbulence models. For the specific application of iceberg capsizing (Fig. 1), two different turbulence equations were tested and were found to give similar results: k-w [Menter, 1993] and Spalart-Allmaras [Spalart and Allmaras, 1992]. The code uses an adaptive grid refinement [Wackers et al., 2012] or an overset meshing method (mandatory to deal with large amplitude body motion close to a wall for example) to connect two non-conforming meshes. The mesh used here is a converged mesh with  $n = 43000$  elements. An example of a typical mesh is illustrated

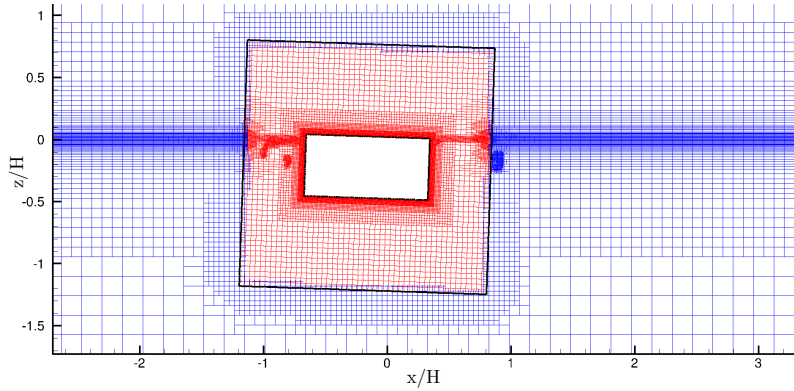


Figure 2: Typical mesh used for the simulation of iceberg capsizing with ISIS-CFD. The two axes represent the dimensionless horizontal position ( $x/H$ ) and the dimensionless vertical position ( $z/H$ ). The iceberg (in white) is in the centre of a squared domain (fine mesh in red) moving with the iceberg inside a background domain (coarser mesh in blue). The mesh is automatically refined around the air-water interface and also around the interface between the two domains to obtain an equivalent cell size around the overlapping region so as to minimize interpolation errors between domains)

in Fig. 2 for an iceberg with  $\varepsilon = 0.5$ . The coupling between the solid and the fluid is stabilized with a relaxation method based on the estimation of the periodically updated added-mass matrix [Yvin et al., 2018].

In the field of application of the ISIS-CFD flow solver, the typical range of Reynolds numbers ( $Re$ , a dimensionless ratio of inertial forces to viscous forces) extends from  $10^6$  for model-scale ship flow to  $10^9$  for full-scale ships [Visonneau et al., 2006]. In this field of ship hydrodynamics, the viscous contribution to the force is as high as 50% of the total force and therefore the scale effect focuses strongly on the prediction of the turbulent boundary layer (relatively thinner in full-scale flows than in model test conditions with delayed flow separation) whereas the scale effect on the free-surface deformation is generally smaller except in the aft-body region due to modification of the pressure field [Mizine et al., 2009].

Here, the ISIS-CFD solver is applied to a significantly different geometry, type of motion and dimensions i.e. to the modelling of the capsizing of rectangular structures with a typical dimension of one kilometre, such as icebergs. This application provides new challenges for the ISIS-CFD solver: high Reynolds numbers  $Re \approx 10^9$ , greater lengths and velocities together with massive separations, high vorticity and free surface motion.

### 2.3 Laboratory experiments conducted by [Burton et al., 2012]

Since ISIS-CFD simulations will be compared with laboratory data (Sections 2.4 and 2.5), we summarize here the technical details of the corresponding experiments conducted by [Burton et al., 2012]. The experimental results presented below were kindly provided by J.C. Burton.

The laboratory experiments consist in the capsizing of parallelepipedic plastic iceberg proxies of density  $\rho_i = 920 \pm 1 \text{ kg/m}^3$  in a long and narrow fjord-like tank 244 cm long, 28 cm wide and 30 cm tall, filled with water at room temperature ( $\rho_w = 997 \text{ kg/m}^3$ ). To assess the effect of water depth  $H_w$  on iceberg-capsize dynamics, two types of experiments were conducted in which the water height was varied from 11.4 cm to 24.3 cm. The iceberg height was  $H = 10.3 \text{ cm}$ , ( $H < H_w$ ) and the width varied between  $W = 2.5 \text{ cm}$  and  $W = 10.2 \text{ cm}$ , corresponding to aspect ratios  $\varepsilon = W/H$  ranging between 0.25 and 1 (see Fig. 1). The length of the iceberg was  $L = 26.6 \text{ cm}$ , which is slightly smaller than the tank width to reduce edge effects so that the flow can be considered as two-dimensional. The plastic icebergs were initially placed slightly tilted with respect to the vertical position and were held by hand close to hydrostatic equilibrium. When the surface of the water became still, several drops of dye were introduced around the plastic iceberg to visualize the water flow. Then the icebergs were released to capsized freely. The capsizes were recorded by a camera located outside the tank. Snapshots are shown in Fig. 3 (top row). Further experimental details can be found in [Burton et al., 2012]. A selection of four experiments are presented here, corresponding to aspect ratios  $\varepsilon = 0.246$ ,  $\varepsilon = 0.374$ ,  $\varepsilon = 0.496$  and  $\varepsilon = 0.639$ .

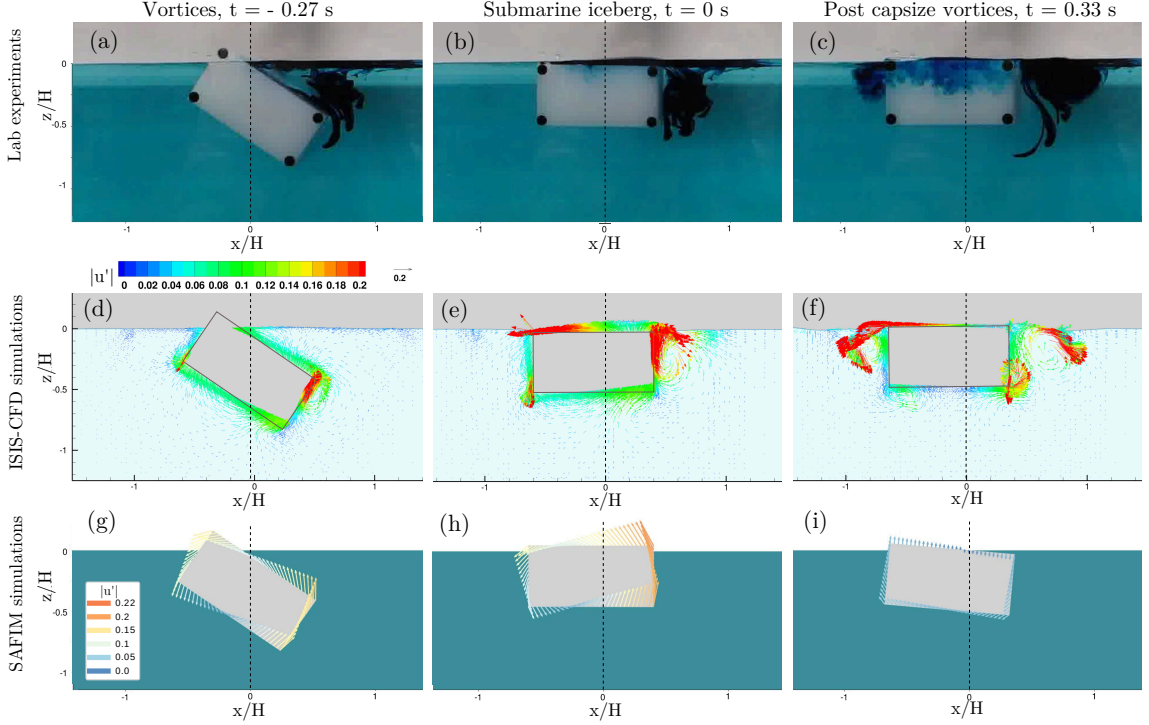


Figure 3: Side view of experiments from [Burton et al., 2012] in the top row (a, b, c); colour map of the dimensionless velocity  $u' = \mathbf{u}/\sqrt{gH}$ , where  $\mathbf{u}$  is the velocity field of the fluid, in the water with ISIS-CFD simulations in the middle row (d, e, f); dimensionless velocity along the surface of the iceberg with SAFIM simulations in the bottom row (g, h, i), for three moments of the capsize (indicated on top of each column). The time scale is calibrated such that  $t = 0$  s corresponds to the first time when the iceberg reaches  $\theta = 90^\circ$ , as in [Burton et al., 2012]. The iceberg aspect ratio is  $\varepsilon = 0.496$ . The floor and walls are not shown in the snapshots. An animated figure computed by ISIS-CFD is available in supplementary material [S1].

## 2.4 Description of fluid motion around capsizing icebergs with ISIS-CFD and laboratory experiments

We assess the patterns of the fluid motion around a capsizing iceberg. Laboratory experiments show, to some extent, the fluid motion using dye at some specific locations. The ISIS-CFD computational fluid dynamics model makes a valuable contribution to the understanding of the complex motion of the fluid surrounding a capsizing iceberg since it computes the whole velocity field in the fluid. Fluid velocity colour maps computed with ISIS-CFD are qualitatively compared with the images of the laboratory experiments in Fig. 3. We also show maps of the iceberg velocity computed along its surface using the calibrated SAFIM model (see Section 3).

Results for the capsizing of an iceberg of aspect ratio  $\varepsilon = 0.496$  are shown for three different times: in Figs 3(a), 3(d) and 3(g) during capsizing; in Figs 3(b), 3(e) and 3(h) just at the end of the capsizing when the iceberg reaches the horizontal position for the first time ( $\theta = 90^\circ$ ); and in Figs 3(c), 3(f) and 3(i) some time after the capsizing. The arrows represent the dimensionless velocity  $|u'| = |\mathbf{u}|/\sqrt{gH}$ , where  $\mathbf{u}$  is the velocity field of the fluid. We observe a good qualitative agreement between the position and inclination of the iceberg obtained by ISIS-CFD and the laboratory experiments. Note that the iceberg is submarine when it reaches  $\theta \approx 90^\circ$  for the first time (Figs 3b and 3e). The motion of the fluid - initially at rest - is visible all around the capsizing iceberg. At a distance of  $H/2$ , the fluid velocity is typically 1.5 cm/s (Fig. 3d). Large vortices, associated with the iceberg motion, are clearly visible throughout the capsizing in Fig 3 (top and middle row). The intense fluid motion represents an important source of energy dissipation and thus slows down the motion of the iceberg. Note also that the iceberg moves towards the left during capsizing. Quantitative observations are given in the next section.

## 2.5 Comparison of ISIS-CFD with laboratory experiments

We will now quantitatively compare ISIS-CFD with the laboratory experiments by [Burton et al., 2012]. In Fig. 4, results are provided for three different unstable icebergs: a thin

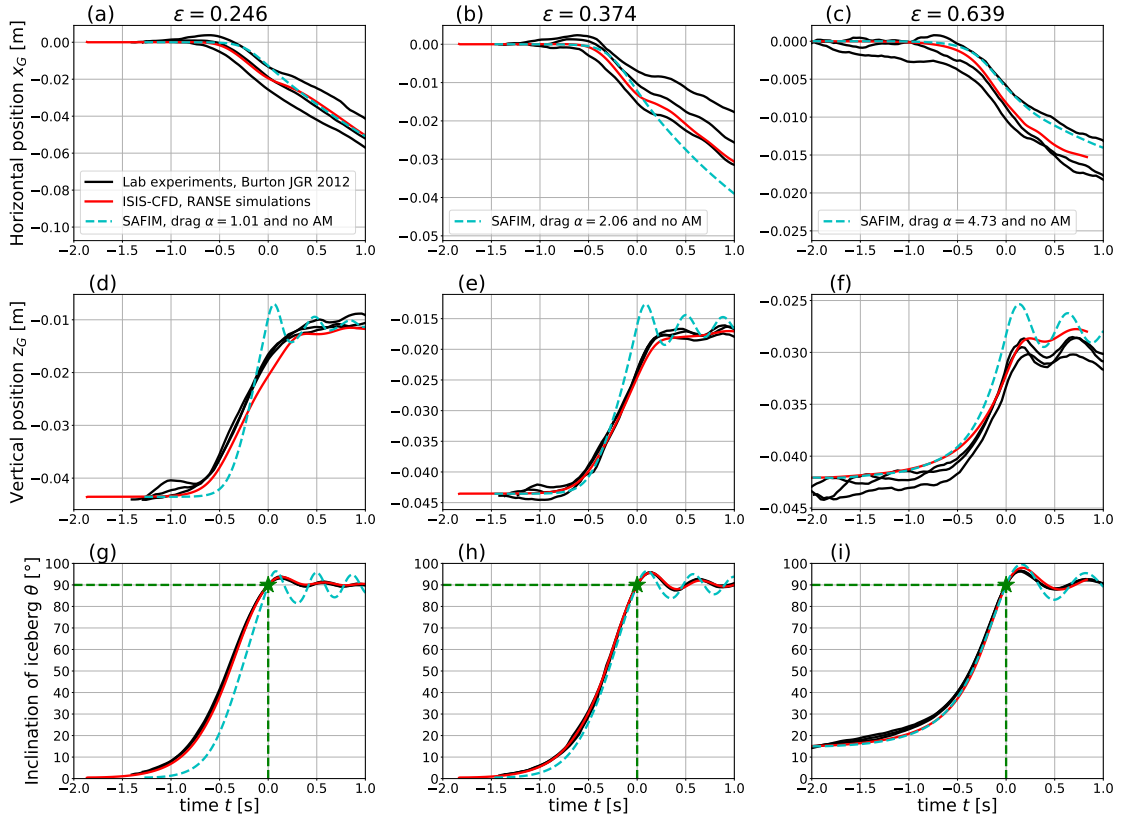


Figure 4: Horizontal position  $x_G$  in the top row (a, b, c), vertical position  $z_G$  in the middle row (d, e, f) and tilt angle  $\theta$  in the bottom row (g, h, i) of icebergs of height  $H = 10.3$  cm for the  $\varepsilon = 0.246$  iceberg in the first column (a, d, g),  $\varepsilon = 0.374$  iceberg in the middle column (b, e, h) and  $\varepsilon = 0.639$  iceberg in the third column (c, f, i). Data are provided for three laboratory experiments (solid black), ISIS-CFD simulations (solid red) and SAFIM simulations (dashed blue). The origin of the time axis in all experiments and simulations is set to the time at which the iceberg reaches the horizontal position for the first time, i.e. when  $\theta = 90^\circ$  (green stars and dashed lines), as in [Burton et al., 2012]

$\varepsilon = 0.246$  iceberg, a medium  $\varepsilon = 0.374$  iceberg and a thick  $\varepsilon = 0.639$  iceberg. The horizontal position  $x_G$ , vertical position  $z_G$  and tilt angle  $\theta$  are plotted against time. As the plastic icebergs were initially positioned by hand, [Burton et al., 2012] observed some variability in the experimental initial conditions and the overall results. To provide an estimate of the variability of the protocol, three experiments with identical plastic icebergs and the same (nominal) initial conditions were conducted for each aspect ratio. We selected these three aspect ratios because of the consistency of the experimental results. For example, for the  $\varepsilon = 0.496$  iceberg (studied in Section 2.4), one of the three laboratory experiments showed a change in direction of the horizontal motion during the capsizing, probably due to an initial non-zero horizontal velocity in a direction opposite to that induced by the rotational motion. For this reason, the set of experiments for the iceberg with  $\varepsilon = 0.496$  was not considered here.

The initial conditions in ISIS-CFD were chosen to fit within the variability of the laboratory experiments. In ISIS-CFD simulations, the icebergs were tilted by a small angle of  $0.5^\circ$  for the thin and medium iceberg (black curves in Figs 4d, 4e) and a larger angle of  $15^\circ$  for the thicker iceberg (black curves in Fig. 4i). The icebergs were initially placed in hydrostatic equilibrium. The water level in the tank  $H_w = 11.4$  cm or  $H_w = 24.3$  cm was found to have a negligible effect on the iceberg motion: results are within the data variability shown in Fig. 4. Therefore, the experiments with a constant water depth  $H_w = 24.3$  cm are presented and this water level was set as a boundary condition in ISIS-CFD simulations.

We first analyse the motion of the iceberg during capsizing. The iceberg is initially slightly tilted with respect to the vertical position and is in hydrostatic equilibrium. Once released, it tilts to reach the horizontal position with associated upward and sideward motion. It then rises out of the water in a rocking motion superimposed with a continuous horizontal displacement (Fig. 4). The thinner the iceberg, the quicker it moves in the horizontal direction with a quasi constant velocity

at least for the first 1.5 s. Indeed, between time  $t = -0.5$  s (beginning of the horizontal motion) and time  $t = 1.0$  s, the icebergs move horizontally by a distance of about  $d = 5$  cm for a  $\varepsilon = 0.246$  iceberg Fig. 4(a),  $d = 3$  cm for a  $\varepsilon = 0.374$  iceberg Fig. 4(b) and  $d = 1.5$  cm for a  $\varepsilon = 0.639$  iceberg Fig. 4(c). This horizontal motion is an important aspect of the iceberg capsize that we would like to focus on here. Note that, besides gravity and buoyancy, the only horizontal external force acting on the capsizing iceberg is a force coming from the relative motion of water around the iceberg (air has a negligible effect here). These hydrodynamic forces are responsible for the horizontal iceberg motion. They need to be captured accurately by the model as they contribute considerably to the contact force generated between the iceberg and the glacier front when a just-calved iceberg capsizes [Tsai et al., 2008, Sergeant et al., 2018].

Fig. 4 shows that ISIS-CFD results are in very good agreement with the laboratory data. For the studied icebergs with three different aspect ratios, all the values of the horizontal movement of the centre of gravity of the icebergs Figs. 4(a), 4(b) and 4(c) computed by ISIS-CFD fit within the range of the laboratory data. Slightly less accurate results are obtained for the vertical movement. However, results are still very close to the laboratory data. We quantify the discrepancy by calculating the relative error on ISIS-CFD data with respect to the closest laboratory data, each time the ISIS-CFD data is outside the laboratory data range. The maximum error is 2.7% and is reached for the vertical motion of the thinnest iceberg (Fig. 4d). For the vertical motion of the two thicker icebergs (e) and (f) and for the inclination of all three icebergs (Figs 4g, 4h and 4i), the error is lower than 1%. This error quantification is conservative since we do not take into account uncertainties on each laboratory measurement.

This slight discrepancy on the vertical and rotational motion computed by ISIS-CFD could be due to differences between the laboratory and simulation set-ups with regards to the 2-dimensional approximation (see section 5.6) and the initial conditions as discussed above. Another reason for this slight discrepancy could be related to the turbulence model treated by a RANS approach. Even if the generation of large vortices and separations are not initially induced by turbulent phenomena (Euler approach captures similar flow topologies), their evolution can be affected by turbulent effects for which the RANS approach is not specifically designed for.

## 2.6 From laboratory scale to field scale

In the previous section, ISIS-CFD simulations were shown to fit laboratory experiments very well. However, our aim is to reproduce the dynamics of the capsize of field-scale icebergs with dimensions of several hundred metres, *i.e.* four orders of magnitude larger than for the laboratory scale. Also, as pointed out by [Sergeant et al., 2018], the laboratory-scale Reynolds number  $Re = LU/\nu \approx 10^3$ , is 6 orders of magnitude smaller than the characteristic Reynolds number  $Re \approx 10^9$  for the field scale (with  $L$  the typical length,  $U$  the typical speed and  $\nu$  the dynamic viscosity of the fluid). Global viscous effects are expected to be more pronounced for laboratory-scale than for field-scale capsize. Therefore, the question is whether laboratory-scale experiments can be used to understand the kinematics of the field-scale iceberg calving.

We compare the horizontal force applied to the iceberg during its capsize computed by ISIS-CFD for the two cases: (1) a field-scale iceberg of height  $H = 800$  m and (2) a laboratory-scale iceberg of height  $H = 0.1$  m, all other parameters being the same: aspect ratio  $\varepsilon = 0.25$ , infinite water pool, same densities of the water, the ice and the air, taken to be equal to the field densities (Section 2.1). Results are given in Fig. 5 using dimensionless variables, *i.e.* a dimensionless horizontal force  $F'_x = F_x/(mg)$  acting on the capsizing iceberg and a dimensionless time  $t' = t/\sqrt{H/g}$ . We observed that the two curves corresponding to the two scales are very similar from the beginning of the movement until  $t' \approx 15.3$ , which corresponds to  $\theta \approx 90^\circ$ . This similarity between the forces at the laboratory and field scales can be explained using the Vaschy-Buckingham  $\pi$  theorem, assuming that the effect of viscosity is negligible, as detailed in Appendix A. After the buoyancy driven capsize, *i.e.* for times larger than  $t' \approx 15.3$ , the discrepancy between laboratory and field scales is larger and dimensions start to play a more important role. This discrepancy probably originates from the fact that after the buoyancy driven capsize, the iceberg motion is driven by the evolution of complex vortices and different gravity-waves dynamics. The other variables of the system (vertical force and torque acting on the iceberg and horizontal and vertical displacement and inclination of the iceberg) are also very similar for the laboratory and field scales.

Since it was demonstrated that the laboratory and field scales produce the same horizontal dimensionless force, in the remaining simulations we will present only the results for the laboratory-scale iceberg with  $H = 0.103$  m and for densities in the field and in absence of sea floor. The laboratory scale was chosen because numerical convergence is easier to achieve in ISIS-CFD for the laboratory scale than for the field scale. The sensitivity of the capsize to the densities will

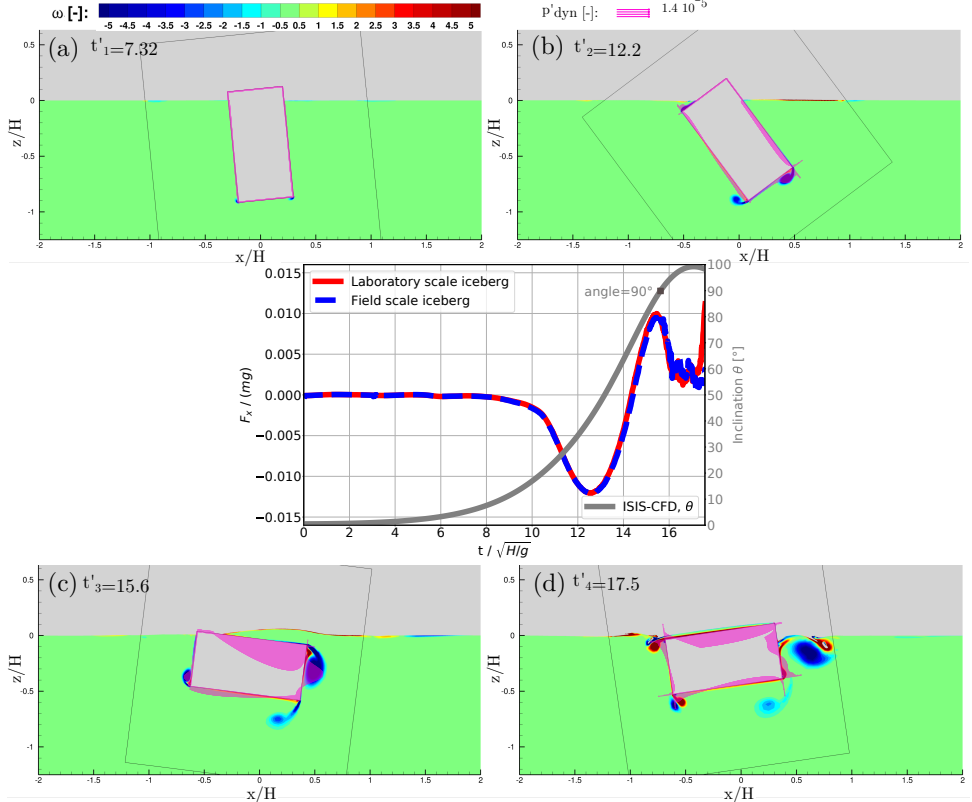


Figure 5: The horizontal dimensionless force  $F' = F_x/(mg)$  that the water exerts on the iceberg is plotted against a dimensionless time  $t' = t/\sqrt{H/g}$  for both laboratory ( $H = 0.1$  m, in red) and field ( $H = 800$  m, in blue) scales. The iceberg inclination  $\theta$  (grey curve with scale on the right) is plotted against dimensionless time  $t'$ . The vorticity fields around the iceberg at four different times are also shown: (a) corresponds to the initial phase of iceberg's motion  $t/\sqrt{H/g} \approx 7.3$ , (b) corresponds to the maximal force in the left direction  $t/\sqrt{H/g} \approx 12.2$ , (c) corresponds to the maximal force in the right direction  $t/\sqrt{H/g} \approx 15.6$  and (d) at time  $t/\sqrt{H/g} \approx 17.1$ , corresponds to the oscillations of the iceberg after complete capsizing. The pink vectors represent the local hydrodynamic pressure. The colour maps are discussed in Section 5.3

Variable name	Dimensionless variable
horizontal force	$F'_x = \frac{F_x}{mg}$
vertical force	$F'_z = \frac{F_z}{mg}$
torque	$M'_\theta = \frac{M_\theta}{mgH}$
horizontal position of G	$x'_G = x_G/H$
vertical position of G	$z'_G = z_G/H$
iceberg inclination	$\theta' = \theta$
time	$t' = t/T_H$

Table 1: Table of dimensionless variables, with  $N'$  denoting the dimensionless variable related to  $N$  and with the iceberg linear mass density  $m = \rho_i H^2 \varepsilon$ , G the center of gravity of the iceberg and the characteristic time  $T_H = \sqrt{H/g}$ . Note that the dimensionless forces and moments can also be written through a normalization by the characteristic mass  $m$ , length  $H$  and time  $T_H$  with the following formulas:  $F'_x = F_x T_H^2 / (mH)$ ,  $F'_z = F_z T_H^2 / (mH)$  and  $M'_\theta = M_\theta T_H^2 / (mH^2)$ . See Section 5.5 for a discussion on a non-dimensionalization with a dimensionless time  $T_{\rho, H}$  that depends on the densities.

be discussed in Section 5.5. Also, the depth of the sea floor was observed to have no effect on the capsize dynamics. Results for icebergs with different heights can be deduced with a factor of proportionality given by the non-dimensionalization in Table 1.

In ISIS-CFD simulations and laboratory experiments, we observe five stages during the capsize:

1. In the *initial* phase ( $0 < t' < 6$ ), the horizontal force  $F'_x$  oscillates around zero with a negligible amplitude: about 1% of its extremum amplitude. This stage is the initiation of the capsize with buoyancy and gravity forces making the iceberg rotate and rise.
2. Then the absolute value of  $F'_x$  increases, first slowly and then faster until the first extremum at  $t' \approx 12.2$ . This is explained by the fact that the induced vertical and rotational velocities and accelerations of the iceberg produce a resisting hydrodynamic fluid force that has a non-zero horizontal component. The horizontal component of this hydrodynamic force is the only horizontal force acting on the iceberg and it induces a horizontal motion of the iceberg.
3. The absolute value of  $F'_x$  decreases to  $F'_x = 0$  before  $t' \approx 14.4$ , which corresponds to  $\theta \approx 70^\circ$  (Fig. 5). This can be explained by the fact that the horizontal motion of the iceberg (explained in phase ii) triggers a horizontal resisting fluid force that compensates part of the hydrodynamic force (mentioned in phase ii).
4. The force  $F'_x$  then becomes positive and increases to an extremum at  $t' \approx 15.6$ , where the iceberg is horizontal  $\theta = 90^\circ$ .
5. In the post-capsize phase (after  $t' \approx 15.6$ ),  $F'_x$  oscillates around zero and is slowly damped to vanish at  $t \gg 15$ . The iceberg rocks around  $\theta = 90^\circ$  and drifts to the left.

The highest water velocities in the surrounding ocean are reached when the iceberg is close to  $\theta = 90^\circ$ . The values of the dimensionless velocities around the iceberg are shown in Fig 6. We observe that for an iceberg of height  $H$  (here 800 m) :

- the water flows at an average speed of  $\approx 0.01 \sqrt{gH}$  (here  $\approx 88$  cm/s) at a distance of about  $H$  (here 800 m) from the iceberg.
- the water flows at the average speed of  $\approx 0.0005 \sqrt{gH}$  (here  $\approx 4.4$  cm/s) at a distance of about  $3.5H$  (here 2800 m) of the iceberg.
- the highest velocity in the fluid during capsize is  $\approx 0.5 \sqrt{gH}$  (here  $\approx 42$  m/s) and is reached by the fluid close to the iceberg.

Moreover, we observe that the iso-lines for the velocities are roughly semi-circles centred on the iceberg, with a radius slightly higher in horizontal direction.

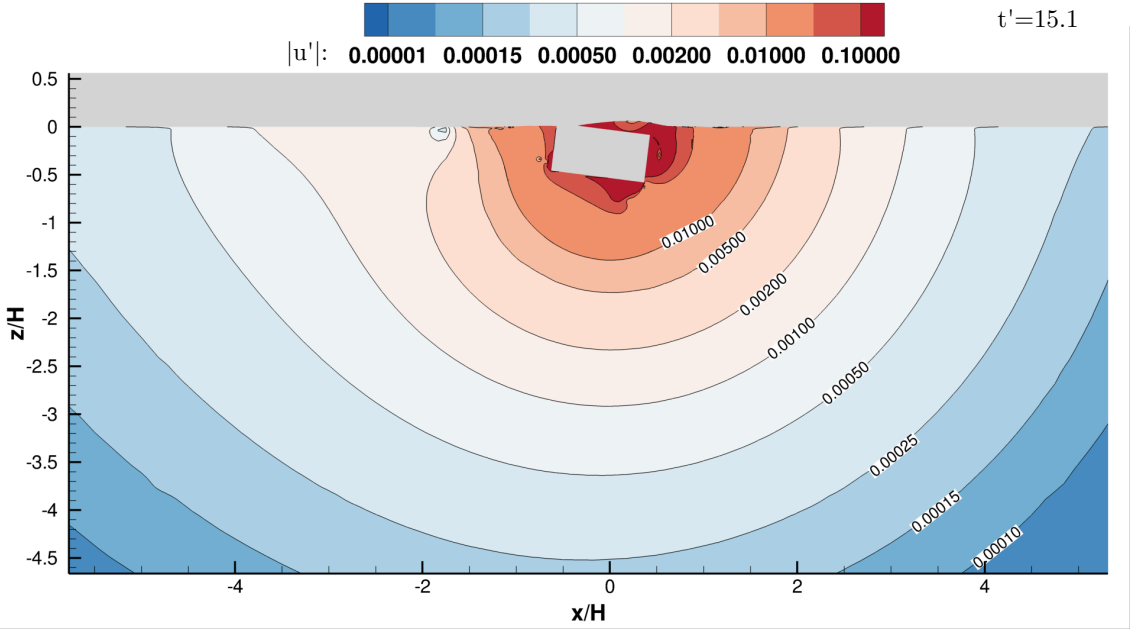


Figure 6: Iso-lines of the absolute value of the dimensionless velocity  $|u'| = |u|/\sqrt{gH}|$  in the fluid surrounding the iceberg with aspect ratio  $\varepsilon = 0.25$  (grey rectangle) at  $t' = 15.1$ . An animated figure is available in supplementary material [S2].

### 3 Semi-Analytical Floating Iceberg Model (SAFIM): an improved empirical model

#### 3.1 General formulation for simplified models

The reference ISIS-CFD model has the advantage of being very accurate for fluid-structure interactions but it cannot readily model contacts between deformable solids. As explained in the introduction, we aim to construct a simpler fluid-structure interaction model that can be more easily coupled with dynamic solid mechanics models. Thus we propose a simple empirical model that can be used to estimate the horizontal force applied to a capsizing iceberg. This model was initiated by the work of [Sergeant et al., 2018, Sergeant et al., 2019] and is extended and validated in this study.

One possible way to construct such a simple model of a capsizing iceberg, used in [Tsai et al., 2008], [Burton et al., 2012] and [Sergeant et al., 2018], consists in solving equations of a rigid iceberg motion subject to relevant forces and moments while discarding water motion. The problem is then greatly simplified at the expense of this strong approximation. The general equations of iceberg motion for such simplified models can be written in two dimensions as:

$$(m + m_{xx})\ddot{x}_G + m_{xz}\ddot{z}_G + J_{x\theta}\ddot{\theta} = \mathbf{F}_d \cdot \mathbf{e}_x \quad (1)$$

$$m_{xz}\ddot{x}_G + (m + m_{zz})\ddot{z}_G + J_{z\theta}\ddot{\theta} = (\mathbf{F}_g + \mathbf{F}_s + \mathbf{F}_d) \cdot \mathbf{e}_z \quad (2)$$

$$J_{x\theta}\ddot{x}_G + J_{z\theta}\ddot{z}_G + (I + I_{\theta\theta})\ddot{\theta} = (\mathbf{M}_s + \mathbf{M}_d) \cdot \mathbf{e}_y \quad (3)$$

where  $I = \rho_i H^4 \varepsilon (1 + \varepsilon^2)$  is the moment of inertia of the iceberg with respect to its centre of mass  $G$  and around an axis parallel to  $\mathbf{e}_y$  (multiplying by the iceberg thickness along  $\mathbf{e}_y$  gives the inertia for the three-dimensional case). Such a formulation accounts for the hydrostatic force  $\mathbf{F}_s$  and the corresponding torque  $\mathbf{M}_s$  computed at the centre of gravity  $G$ , the gravity force  $\mathbf{F}_g$ , overall hydrodynamic (or drag) effects expressed by the force  $\mathbf{F}_d$  and the associated torque  $\mathbf{M}_d$  and so-called added-masses  $m_{xx}$ ,  $m_{zz}$ ,  $I_{\theta\theta}$ ,  $m_{xz}$ ,  $J_{z\theta}$  and  $J_{x\theta}$  that account for the mass of water that must be displaced during the iceberg motion (the added-masses will be discussed below). We also define the total forces and torque (including the action of the added-mass) on each coordinate: the horizontal force is  $F_x = m \ddot{x}_G$ , the vertical force is  $F_z = m \ddot{z}_G$  and the torque is  $M_y = I \ddot{\theta}$ .

Hydrodynamically induced forces that oppose the motion of solids in a fluid are commonly called "drag forces"  $\mathbf{F}_d$  and the corresponding drag moment  $\mathbf{M}_d$  accounts for a particular distribution of the drag pressure along the solid. The drag force is usually normalized by the squared relative velocity between the fluid and the solid with a factor of fluid density and it acts in the opposite

	Added-mass (AM):	Pressure drag:
Tsai et al. (2008)	$m_{xx_T} = \frac{3\pi\rho_w L}{8} (H^2 \cos(\theta)^2 + W^2 \sin(\theta)^2)$ $m_{zz_T} = 0$ $I_{\theta\theta_T} = \frac{\rho_w}{24} (H^2 - W^2)^2$ $m_{xz} = 0, J_{x\theta} = 0, J_{z\theta} = 0$	$\mathbf{F}_d = 0$ $\mathbf{M}_d = 0$
Burton et al. (2012)	$m_{xx} = 0$ $m_{zz} = 0$ $I_{\theta\theta} = 0$ $m_{xz} = 0, J_{x\theta} = 0, J_{z\theta} = 0$	$\mathbf{F}_{d_B} \cdot \mathbf{e}_x = \nu_x  \dot{x} ^2 \text{sign}(\dot{x})$ $\mathbf{F}_{d_B} \cdot \mathbf{e}_y = \nu_y  \dot{y} ^2 \text{sign}(\dot{y})$ $\mathbf{M}_{d_B} \cdot \mathbf{e}_z = \nu_z  \dot{\theta} ^2 \text{sign}(\dot{\theta})$

Table 2: Dynamic fluid forces proposed by [Tsai and Ekström, 2007] and [Burton et al., 2012] for iceberg capsize modelling

direction of this velocity. A comparison between the pressure drag and the negligible friction drag is discussed in Appendix 5.3.

When the fluid motion is not computed, the added-mass (AM) should also be included in the model. Added-masses add some additional inertia to the moving solid. This effect is known to be significant when the density of the solid and the fluid are comparable, such as for ice and water. The matrix of added-masses, which is symmetrical [Yvin et al., 2018, Molin, 2002], has the following form:

$$[m_{AM}] = \begin{bmatrix} m_{xx} & m_{xz} & J_{x\theta} \\ m_{xz} & m_{zz} & J_{z\theta} \\ J_{x\theta} & J_{z\theta} & I_{\theta\theta} \end{bmatrix} \quad (4)$$

Added-mass effects are of two types. First, a force associated with an added-mass can arise in a given direction due to an acceleration in that direction, which corresponds to the *diagonal* terms  $m_{xx}$ ,  $m_{zz}$  and  $I_{\theta\theta}$  in Eq. (1-3). Second, an added-mass force can arise in a given direction due to an acceleration in another direction, which is accounted for by the *coupled* terms  $m_{xz}$ ,  $J_{z\theta}$ ,  $J_{x\theta}$ .

Within this framework, models proposed by [Burton et al., 2012] and [Tsai et al., 2008], summarized in Table 2, differ in the way they account for the drag and the added-mass. In the formulation proposed by [Tsai et al., 2008], pressure drag and the associated moment are not considered and only some of diagonal terms are taken into account in the added-mass matrix. In the formulation by [Burton et al., 2012], added-mass effects are neglected. As for the drag effects, they are assumed to depend only on individual components of the velocity of the centre of gravity  $G$  and on the angular velocity, for example the drag along  $\mathbf{e}_x$  only depends on the velocity  $\dot{x}_G$ . As a consequence, both models predict that an iceberg initially at rest ( $\dot{x}_G = 0, \ddot{x}_G = 0$ ) will not experience any horizontal movement along  $\mathbf{e}_x$  during its capsize. As discussed above, this result contradicts experimental and ISIS-CFD results.

### 3.2 SAFIM: a new capsize model

To improve the above mentioned simplified models, we have developed a new model that continues along the lines of previous propositions by our group [Sergeant et al., 2018, Sergeant et al., 2019]. In addition to the previously used drag formulation, this model uses a drag coefficient varying with the aspect ratio and integrates added-mass effects. As will be shown, SAFIM reproduces the main results of ISIS-CFD. For example, it predicts the horizontal movement of capsizing icebergs initially at rest.

A particular feature of the drag model in SAFIM is that it is based on the local velocity of the iceberg's surface. Therefore, the total drag force and the drag moment, evaluated as integrals of local pressure and moment over the submerged part of the iceberg  $\Gamma_s$ , is described as:

$$\mathbf{F}_d = -\alpha \frac{1}{2} \int_{\Gamma_s} \rho_w v_n^2 \text{sign}(v_n) \mathbf{n} d\Gamma, \quad (5)$$

$$\mathbf{M}_d = -\alpha \frac{1}{2} \int_{\Gamma_s} v_n^2 \text{sign}(v_n) (\mathbf{r} - \mathbf{r}_G) \wedge \mathbf{n} d\Gamma, \quad (6)$$

where  $\mathbf{n}$  is the local normal to the surface of the iceberg and  $v_n = |\mathbf{v} \cdot \mathbf{n}|$  is the normal velocity,  $\mathbf{r}$  is the local position vector and  $\mathbf{r}_G$  is the position vector of the iceberg's centre of mass; the wedge  $\wedge$  denotes a vector product. We consider a quadratic dependence of the local drag force on

the normal velocity in the following. See Section 5.3 for a discussion of various drag models. The integral expressions for the drag force and moment are given in Appendix B.

The factor  $\alpha$  is the only adjustable parameter of the drag model. It can be used to adjust the model with respect to the reference ISIS-CFD simulations. We recall that in the original papers of [Sergeant et al., 2018, Sergeant et al., 2019], this factor  $\alpha$  was set to  $\alpha = 1$  by default. However, due to the complexity of the fluid flow, the optimal value of  $\alpha$  may change with the geometry of the iceberg.

This formulation, rather than attempting to describe the local pressure accurately, which is difficult based on geometrical considerations only (see [Sergeant et al., 2018] and Section 5.3), aims at providing a good approximation of the global forces and moments acting on the rotating iceberg. As opposed to the simplified drag model of [Burton et al., 2012], in which the drag force and moment depend only on the velocity of the centre of gravity, in this formulation the hydrodynamic forces  $\mathbf{F}_d$  and the torque  $\mathbf{M}_d$  depend on the iceberg's current configuration  $x_G, z_G, \theta$  and on the three velocities  $\dot{x}_G, \dot{z}_G, \dot{\theta}$ , since the local velocity  $v_n$  is a function of all six state variables. This makes it possible to produce a horizontal force acting on the iceberg during capsizing even for icebergs initially at rest. Another advantage is that a unique fit-parameter  $\alpha$  is required to represent the drag effect, contrary to three independent fit parameters used in [Burton et al., 2012]. This makes it possible to easily generalize the model to more complex iceberg geometries. The closed form expressions of the drag forces and the moment are given in Appendix B.

As for the added-masses in SAFIM, we will consider two different possibilities: *simplified* added-masses and *computed* added-masses.

The *simplified* added-masses option is based on analytical formulas for the diagonal terms of the added-mass matrix. The coupled terms of added-mass are taken to be equal to zero:  $m_{xz} = 0$ ,  $J_{z\theta} = 0$ ,  $J_{x\theta} = 0$ . The formulas used are taken from [Wendel, 1956] for fully or partly submerged solids and were adapted to a capsizing body. The horizontal and vertical added-masses take the following forms:

$$m_{xx} = \frac{1}{4} C_x \pi \rho_w H_{\text{eff}}^2 \quad (7)$$

$$m_{zz} = \frac{3}{16} C_z \pi \rho_w W_{\text{eff}}^2 \quad (8)$$

where  $H_{\text{eff}}$  and  $W_{\text{eff}}$  are the effective height and width defined as the projection of the submerged part of the iceberg along the vertical and horizontal axes, respectively (see Fig. 1). The integral equations of the simplified added-masses  $m_{xx}$  and  $m_{zz}$  are given in Appendix B. The effective height and width depend on the vertical and angular positions of the iceberg that evolve during the capsizing. Therefore  $m_{xx}$  and  $m_{zz}$  also evolve during the capsizing. On the other hand, the added moment of inertia  $I_{\theta\theta}$  is assumed to depend only on the height of the iceberg, so it remains constant during the capsizing:

$$I_{\theta\theta} = 0.1335 C_\theta \pi \rho_w \left(\frac{H}{2}\right)^4 \quad (9)$$

In order to adjust the added-mass effect used in SAFIM to reproduce the reference ISIS-CFD results, we introduce three factors in the above equations:  $C_x$ ,  $C_z$  and  $C_\theta$ . In the next section, we compute the optimal values of these coefficients for various aspect ratios by minimizing the mismatch between SAFIM and ISIS-CFD.

*Computed* added-masses are calculated for each position of the iceberg. This is done by applying a unit acceleration on the iceberg for the considered degree of freedom and solving eqs. (18) and (16) of [Yvin et al., 2018] on the fluid domain using a numerical method such as the finite-element, finite-volume or boundary element method. The integration of the induced pressure field on the body gives the complete column of the symmetrical added-mass matrix corresponding to the considered degree of freedom, with both diagonal and coupled entries. Similarly to the simplified added-mass method, the values of the computed added-mass also depend on the iceberg position and they therefore evolve during the capsizing. For the computed added-masses, the coupled terms are non-zero, giving rise to a coupling between horizontal, vertical and rotational accelerations.

To solve the motion equations (1-3) with SAFIM, the Störmer-Verlet integration scheme is used. Since SAFIM has only three degrees of freedom, the integration over time is very fast, only a few seconds compared to few hours for ISIS-CFD on a single CPU. The time step in SAFIM that ensures a sufficiently accurate results is  $\Delta t = 0.1$  s in the field scale and  $\Delta t = 0.001$  s in the laboratory scale. In both cases, this corresponds to a dimensionless time step of  $\Delta t' = \Delta t / \sqrt{H/g} \approx 0.01$ .

## 4 Performance and limits of SAFIM

### 4.1 Studied cases and methodology for SAFIM coefficient calibrations

The validation of the proposed SAFIM model should be suited to the final objectives: (1) accurate reproduction of the forces exerted on the iceberg during capsize, especially the horizontal component and the moment since they determine the resulting contact force when the iceberg is in contact with the glacier; (2) ease of implementation in a finite element solver for simulation of the whole iceberg-glacier-bedrock-ocean system, (3) suitability of the model for the entire range of possible geometries of icebergs encountered in the field.

In this context, we consider 2D icebergs with rectangular cross-sections (Fig. 1). 3D effects are discussed in Section 5.6. We use typical densities observed in the field (Section 2.1). As will be discussed in Section 5, the considered density has a non-negligible effect on the calving kinetics.

For this study, we select four iceberg geometries with a wide range of aspect ratios: exactly the same four geometries as described in Section 2.3.

A small initial tilt angle is set to  $0.5^\circ$  (except for the thickest iceberg). This does not change the overall motion of the iceberg compared to a zero tilt -i.e. initially vertical iceberg- but it affects the "destabilization" period during which the iceberg slowly rotates or oscillates around its vertical position [Sergeant et al., 2018]. For the thickest iceberg with  $\varepsilon = 0.639$ , the initial tilt angle is  $15^\circ$ . This angle produced ISIS-CFD simulations that best matched the laboratory experiments. Moreover, for the same angle of inclination and height, the initial torque is smaller for larger icebergs [Wagner et al., 2017]. Also,  $\varepsilon = 0.639$  is close to the critical value  $\varepsilon_c = 0.65$  corresponding to the limit for iceberg stability (Section 2.1).

To compare SAFIM and ISIS-CFD results, we compute the mismatch in the time-evolution of the horizontal forces  $F_x$  ( $\mathcal{L}^2$  norm) during the capsize. The phases of the capsize that we focus on are phases (ii) and (iii) (defined in Section 2.6). The reason we do not seek to perfectly model phase (i) with SAFIM is discussed in Section 5.2. Also, SAFIM is designed to model the capsize phase but cannot model the very end of the capsize ( $\theta > 80^\circ$ ), i.e. phase (iv), nor the post-capsize phase (v). In these phases, forces induced by complex fluid motion, which are difficult to parametrize, are expected to dominate gravity and buoyancy forces.

For SAFIM with a drag force and no added-masses, the mismatch can be written:

$$E_1 = \frac{\int_{t_1}^{t_2} |F_{x_{\text{ISIS}}}(t) - F_{x_{\text{SAFIM}}}(t - \Delta t)|^2 dt}{\int_{t_1}^{t_2} |F_{x_{\text{ISIS}}}(t)|^2 dt} \quad (10)$$

with  $F_x$  the total horizontal force acting on the iceberg,  $t_1$  such that  $F_x(t_1) = 1/6F_{\min}$  and  $t_1 < t_{F_{\min}}$  and  $t_2$  such that  $F_x(t_2) = 1/6F_{\max}$  and  $t_2 > t_{F_{\min}}$ , with  $F_{\min}$  the first extremum of the force and  $t_{F_{\min}}$  the time at which it occurs. The SAFIM response is shifted artificially in time so that the first extremum of the curve fits that of ISIS-CFD. This time shift  $\Delta t$  is discussed in Section 5.2.

For the SAFIM model with a drag force and added-masses, the mismatch is written:

$$E_2 = \frac{\int_0^{t_3} |F_{x_{\text{ISIS}}}(t) - F_{x_{\text{SAFIM}}}(t)|^2 dt}{\int_0^{t_3} |F_{x_{\text{ISIS}}}(t)|^2 dt} \quad (11)$$

where  $t = 0$  is the beginning of the simulation and  $t_3$  the first time for which the horizontal force crosses zero  $F_x(t_3) = 0$  after  $t_{F_{\min}}$ . The curve is not shifted in time as for  $E_1$ .

Equations (10) and (11) are computed for a parametric space of drag and added-mass coefficient detailed in Appendix C. The optimized values of the coefficients  $\alpha$ ,  $C_x$ ,  $C_z$  and  $C_\theta$  are chosen such that the errors  $E_1$  and  $E_2$  are minimum.

### 4.2 Effect of drag and added-mass on the iceberg horizontal force

We analyse the horizontal force produced by SAFIM in order to understand the effects of the drag force and added-masses on the dynamics of the iceberg capsize. To do so, the dynamics of an iceberg with an aspect ratio  $\varepsilon = 0.246$  were simulated by SAFIM with or without drag and with or without added-masses (Fig. 7) and compared to the results of ISIS-CFD. We also assessed the sensitivity of the total horizontal force  $F_x$  to the drag coefficient and added-masses in Fig. 7.

First, without the drag and without non-diagonal terms of the added-masses, the horizontal force predicted by SAFIM was equal to zero  $F'_x = 0$ , as expected. Next, we analysed the results of SAFIM with a drag force and without added-masses. Fig. 7 shows the horizontal force computed

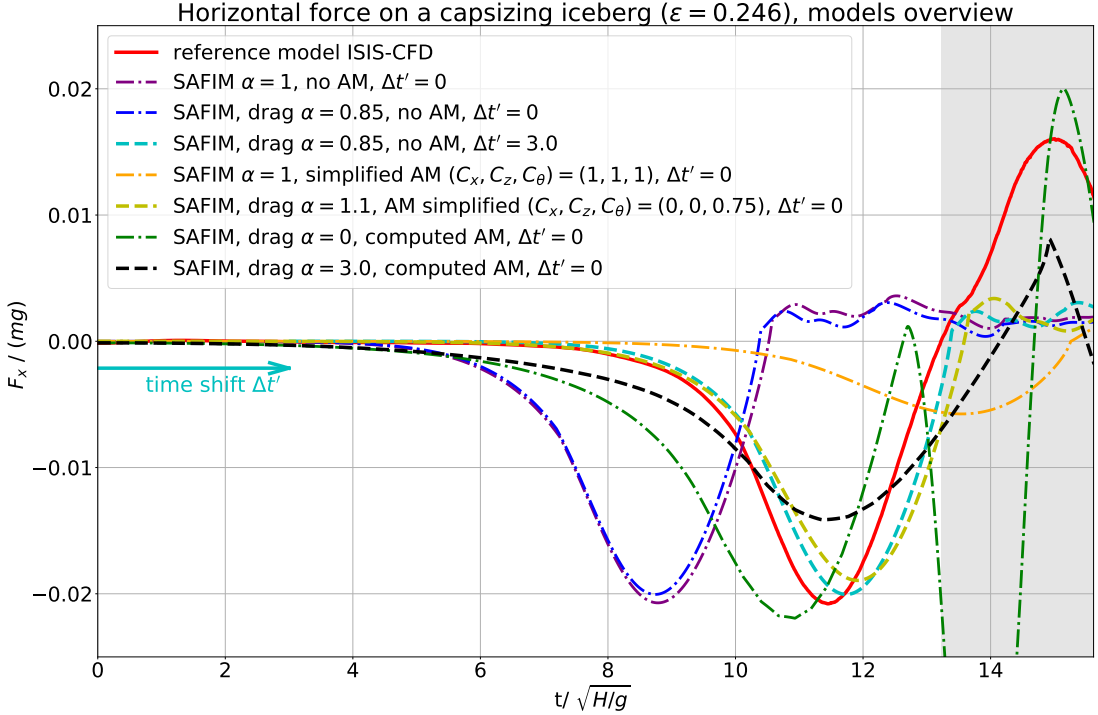


Figure 7: Computed horizontal force  $F'_x = F_x/(mg)$  applied on the iceberg versus dimensionless time  $t' = t/\sqrt{H/g}$  for a reference ISIS-CFD simulation and for SAFIM simulations with different drag and added-mass parameters.

by SAFIM without added-mass for two values of the drag coefficient:  $\alpha = 1$  (purple curve) and  $\alpha = 0.85$  (blue curve). The value  $\alpha = 0.85$  is the optimized value of  $\alpha$  obtained by minimizing the error  $E_1$  (Eq. 10). The force has a slightly higher amplitude (around  $t' \approx 8.5$ ) and duration for SAFIM with  $\alpha = 1$  than with the optimized drag coefficient  $\alpha = 0.85$ . Whatever the value of the drag coefficient, the SAFIM horizontal force curve does not fit the ISIS-CFD curve over time: the amplitude and shape are very similar to the ISIS-CFD results, but the initiation process occurs faster with SAFIM. When the SAFIM curves are shifted in time by  $\Delta t' = 3.0$  (cyan curve in Fig. 7), the previous SAFIM curve (with drag coefficient  $\alpha = 0.85$  and without added-masses) fits the ISIS-CFD curve well. The shape is the same and the error on the waveform is  $E_1 = 5.2\%$ , with a relative error on the first force extremum of 4%.

Then, we analysed the effects of simplified added-masses. The SAFIM simulation with drag and simplified added-mass coefficients all equal to 1 gives horizontal force results that are very different from the reference ISIS-CFD results: the duration of the capsizing is largely overestimated and the amplitude is strongly underestimated (orange curve in Fig. 7). The optimized drag and added-mass coefficients that give a minimum error  $E_2$  are  $\alpha = 1.1$  for the drag,  $C_\theta = 0.75$  for the added moment of inertia and zero added-masses ( $C_x, C_z = (0, 0)$ ). The corresponding results (yellow curve in Fig. 7) are in a very good agreement with the reference results ( $E_2 = 10\%$ ) both for the shape and for the time corresponding to the force extremum  $t' \approx 11.45$  (same as for ISIS-CFD). The added moment of inertia (associated with coefficient  $C_\theta$ ) slows down the initial rotation of the iceberg. However, the amplitude of the extremum is slightly underestimated by 8% compared to that predicted by ISIS-CFD. The accuracy of the formula of the simplified added-masses with coefficients equal to 1 is discussed in section 5.4.

The curve for SAFIM with computed added-masses and no drag force (dark green curve in Fig. 7) gives a curve that fits the reference results quite well in amplitude but not in time and predicts a huge second extremum with the wrong sign (negative instead of positive). However, when correcting the drag coefficient to  $\alpha = 3.0$ , which minimizes the error  $E_2$ , the curve fits better in time, reproducing the initial slow change of the force, but the amplitude and the shape still do not fit (black curve in Fig. 7). Similarly to the simplified added-masses, the computed added-masses slow down the initial rotation of the iceberg.

This analysis suggests that the drag force has mainly an effect on the amplitude of the first force extremum and that the added-masses have an effect on the duration of the initiation of the

capsize. Also, optimized coefficients of drag and added-masses improve the model significantly compared with the case with all coefficients set to 1. Further discussions on the pros and cons of the SAFIM models are given in Section 5.1.

### 4.3 Effect of the iceberg's aspect ratio on SAFIM overall performance

We will now analyse the forces and the torque acting on the four selected geometries of icebergs computed by ISIS-CFD and SAFIM. The evolution of the dimensionless horizontal force  $F'_x$ , vertical force  $F'_z$ , torque  $M'_\theta$ , horizontal displacement  $x'_G$ , vertical displacement  $z'_G$  and inclination  $\theta$  obtained by ISIS-CFD and SAFIM are plotted in Fig. 8 for SAFIM results obtained with drag and without added-masses and in Fig. 9 for SAFIM results with drag and simplified added-masses. SAFIM models use optimized parameters indicated in Table 3 for each aspect ratio.

We will first discuss the sensitivity of the computed forces to the aspect ratios  $\epsilon$ . We observe that the amplitude of the first extremum of both the horizontal force  $F'_x$  and the vertical force  $F'_z$  decreases with increasing aspect ratio. Also, the amplitude of the horizontal acceleration is equal to  $\ddot{x}_G = F_x/m = gF'_x$ , so the horizontal acceleration of the iceberg decreases with increasing aspect ratio. This is consistent with the observed slower horizontal displacement of icebergs with larger aspect ratios as reported in Section 2.5. Also, the durations of the first negative part of the horizontal force and first positive part of the vertical forces are similar for the four aspect ratios: about 5 units of dimensionless time.

The minimal error  $E_1$  of SAFIM with the drag and without added-masses increases with the aspect ratio (from 5% for  $\epsilon = 0.246$  and up to 24% for  $\epsilon = 0.639$ ). We also found that the optimal drag coefficient  $\alpha$  increases in an approximately affine way with the aspect ratio (Fig. 10a) as:

$$\alpha_{\text{opt}}(\epsilon) \approx -1.6 + 8.8\epsilon$$

with the coefficient of determination equal to  $R^2 = 0.98$ . This linear regression is valid within the range of studied aspect ratios  $0.246 \leq \epsilon \leq 0.639$ . Note that this formula should not be used for  $\epsilon < 0.18$  for which the drag coefficient would be negative, which is physically meaningless.

The minimal errors  $E_2$  for SAFIM with the drag and the simplified added-masses are greater than the errors  $E_1$  for SAFIM with drag without added-masses and with the artificial time shift as plotted in Fig. 10(b) for each aspect ratio. As for  $E_1$ , the error  $E_2$  increases with the aspect ratio (from 10% for  $\epsilon = 0.246$  up to 26% for  $\epsilon = 0.639$ ). Note that for all the four studied cases, optimization of the error requires keeping only one non-zero added-mass coefficient: the added moment of inertia coefficient. Indeed, the simplified added-masses are added to reproduce the duration of the force's growth as accurately as possible, without changing the shape of the rest of the force curve that is already well represented by the drag force model. Therefore, the simplified added-masses should allow the slow initiation of the rotation, which can be explained by an added moment of inertia of the surrounding fluid. Moreover, the torque  $M'_\theta$  and the vertical force  $F'_z$  are better represented by SAFIM with simplified added-masses (Fig. 9a) than without added-mass and with an artificial time shift (Fig. 8a) for the four studied geometries.

We also compared SAFIM including drag and the computed added-masses with the reference ISIS-CFD model. This SAFIM simulation predicts the time and amplitude of the extremum of the force and the torque less accurately than the two previous SAFIM simulations: the error  $E_2$  for SAFIM with drag and computed added-masses is  $E_2 > 34\%$  for all the four studied cases (Fig. 10b). The curves for this less accurate model are not shown.

## 5 Discussion

First we will discuss the performance of SAFIM in Sections 5.1 and 5.2, then SAFIM modelling choices in Sections 5.3 and 5.4 and finally the sensitivity of the model to the main geophysical constraints in Sections 5.5, 5.6 and 5.7.

### 5.1 SAFIM performance and comparison with previous models from the literature

The advantages of the formulated and validated SAFIM model with drag and without added-masses is that (1) it can be readily implemented in a finite element model like the one in [Sergeant et al., 2018], (2) it requires only one parameter, the drag coefficient  $\alpha_{\text{opt}}(\epsilon) \approx -1.6 + 8.8\epsilon$ , (3) it quite accurately reproduces the shape and amplitude of the horizontal force with an error that increases with the iceberg aspect ratio from 5% for  $\epsilon = 0.246$  up to 25% for  $\epsilon = 0.639$ . The

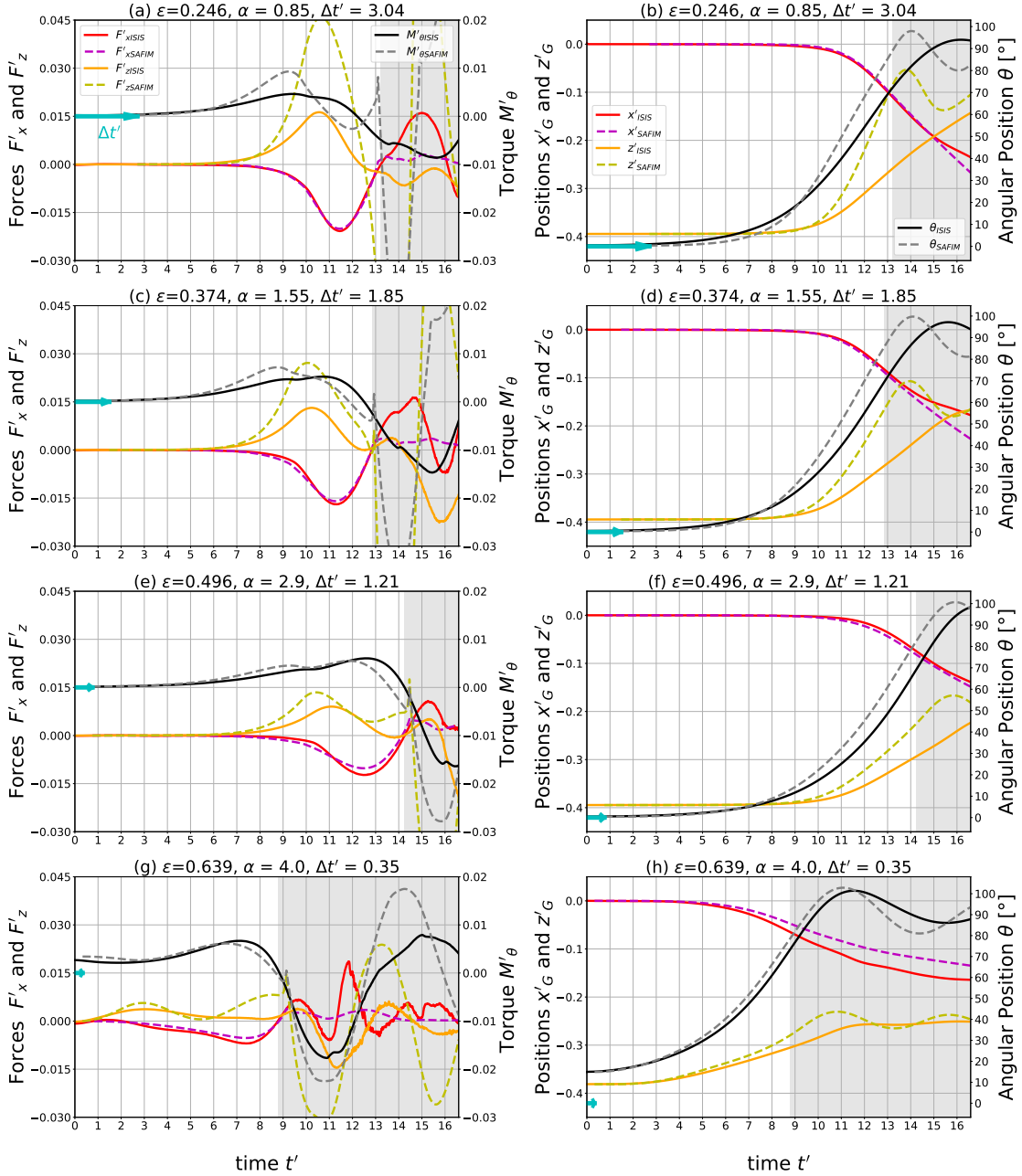


Figure 8: Capsize simulations for SAFIM with drag and without added-masses and for ISIS-CFD: evolution of the dimensionless total horizontal force  $F'_x$ , vertical force  $F'_z$  and torque  $M'_\theta$  on the iceberg (a, c, d, e), of the horizontal  $x'_G$  and vertical  $z'_G$  positions of the centre of gravity  $G$  and of the inclination  $\theta$  of the iceberg (b, d, f, g). Results are given for icebergs with  $\varepsilon = 0.246$  (a, b),  $\varepsilon = 0.374$  (c, d),  $\varepsilon = 0.496$  (e, f) and  $\varepsilon = 0.639$  (g, h). SAFIM curves were shifted (green arrow) by the dimensionless time  $\Delta t' = \Delta t \sqrt{g/H}$ . The SAFIM drag coefficient  $\alpha$  and time  $\Delta t'$  are indicated in the titles.

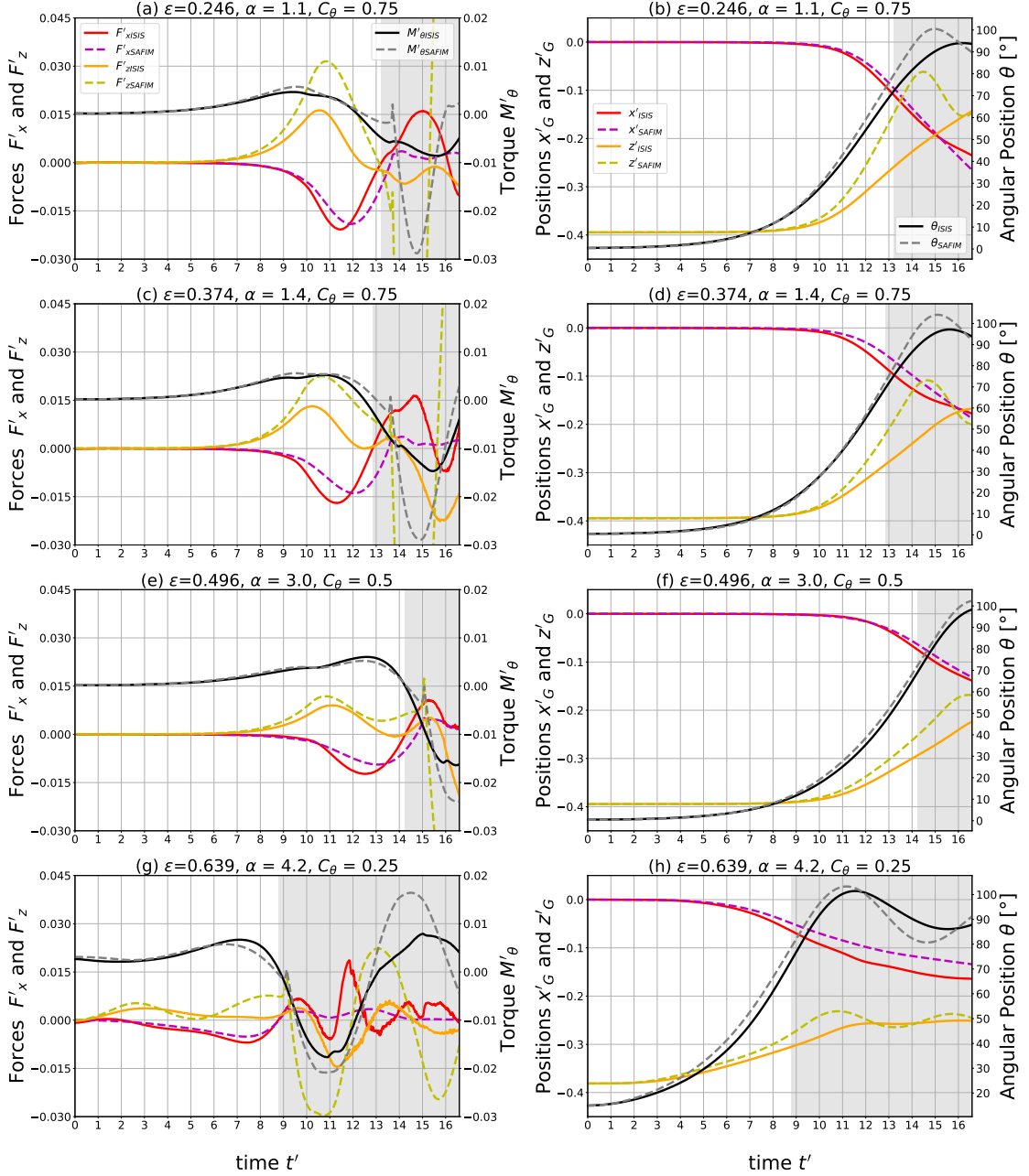


Figure 9: Same as in Fig. 8 but for SAFIM with drag, simplified added-masses and no time shift ( $\Delta t'$ ). SAFIM drag coefficient  $\alpha$  and added-mass coefficient  $C_\theta$  are indicated in the titles.

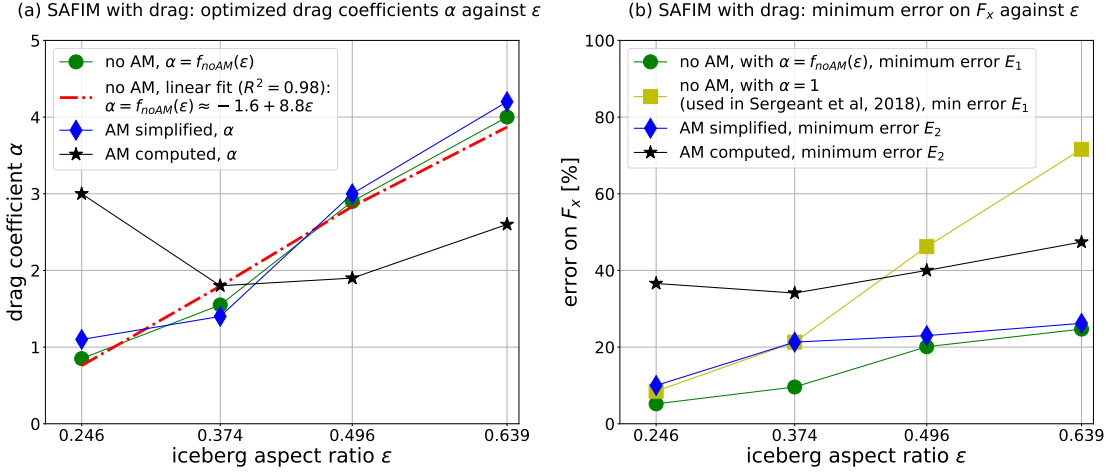


Figure 10: (a) Optimized values of the drag coefficient  $\alpha$  for different iceberg's aspect ratios, which were determined for SAFIM with and without added-mass (AM), only added moment of inertia was used in the simplified added-mass model, and a full added-mass matrix was used for the computed added-mass; (b) the minimal error of the horizontal force corresponding to different models for different iceberg's aspect ratios.

drawback of this model is that it does not correctly simulate the kinetics of the iceberg capsizing, especially the time needed to reach the peak force (see discussion in Section 5.2). In addition, the evolution of the torque and vertical force is not well reproduced. The advantage of SAFIM with drag and simplified added-masses is that it correctly reproduces the time of the force extremum (no shift in time is needed) and it reproduces the torque and the vertical force better than SAFIM with drag and no added-masses. The drawbacks of SAFIM with drag and simplified added-masses is that it underestimates the amplitude of the first force extremum by 10%.

SAFIM with drag and computed added-masses gives less accurate results than the two other SAFIM versions. Considering that the computed added-masses are physical and accurate [Yvin et al., 2018], the drag force given in SAFIM is physically lacking since it does not make it possible to reproduce the dynamics of the iceberg.

Here, we discuss the possible implementation of added-mass in a finite element solver with the aim of reproducing glacier calving behaviours as discussed in [Sergeant et al., 2018, Sergeant et al., 2019]. While adding an arbitrary added-mass matrix is feasible in the framework of dynamics of rigid solids, its use in a finite element framework is not straightforward. As the optimization analysis showed, the only term that needs to be added in the simplified added-masses is the added moment of inertia (Table 3), keeping the total mass and the outer shape of the iceberg unchanged. It is a challenging, if even possible, task to compute such a mass distribution in order to change the inertia of the iceberg accordingly. If such a redistribution of the iceberg density is not possible, the use of simplified added-masses might therefore require adding an external moment on the iceberg at each time step proportional to the acceleration weighted by a factor of the added moment of inertia. Using computed added-masses might also require adding external forces and moments on the iceberg at each time step proportional to the coupled terms of the added-mass matrix. One advantage of computed added-masses over simplified added-masses is that there is no adjustable parameter. However, at every time step, the added-mass matrix should be computed which considerably slows down and complexifies the simulation.

Finally, the proposed SAFIM model well predicts the first part of the horizontal force applied by the fluid on the iceberg, either when using a drag force only (i.e. no added-masses) and shifting the curve in time or when using a drag force and simplified added-masses (and no shift in time). However, the evolution of the force after the capsizing ( $\theta > 80^\circ$ ) is not well modelled by SAFIM. This is probably due to the fact that the evolution of the local pressure force is governed by a complex established fluid motion around the iceberg (see Section 5.3) which is hard to parametrize without full fluid dynamics computations. Given the global aim of modelling seismic waves generated by capsizing icebergs, this part should not play any role as it happens after the loss of the iceberg contact with the glacier front. An advantage of SAFIM over previous models [Tsai et al., 2008, Burton et al., 2012] is that, thanks to a special form of the drag force, it can describe the horizontal movement of a capsizing iceberg triggered by its rotation. As shown

in [Sergeant et al., 2018], SAFIM can distinguish between a top-out and bottom-out capsizing, when used to simulate the contact force between a capsizing iceberg and a rigid wall. A qualitative explanation of the emerging non-zero horizontal force given by the drag force is discussed in Appendix B.

We calculate the error in SAFIM with a drag coefficient  $\alpha = 1$  for all aspect ratios and without added-mass (Fig. 10). Exactly the same model was used in [Sergeant et al., 2018, Sergeant et al., 2019], but for modelling an iceberg capsizing in contact with a glacier. The error  $E_1$  is about two times greater than when taking the optimum value of the  $\alpha$  coefficient for each aspect ratio, and the amplitude and duration of the first negative part of the force is underestimated - except for the thinnest iceberg with  $\varepsilon = 0.246$ , for which the opposite is true, as mentioned in Section 4.2. Note that this error is relevant for a freely capsizing iceberg. In future work, the errors for an iceberg capsizing in contact with a glacier should be estimated but this will require a reference model for fluid-structure interactions that can track the contact between solids, which is a highly challenging problem.

## 5.2 Initiation phase of the capsizing

In the previous sections, the drag parameter  $\alpha$  for SAFIM with a drag force and without added-masses was optimised by implementing an artificial time shift of the SAFIM force curve with respect to the ISIS-CFD force curve. This was done because, as already mentioned, SAFIM without added-masses is not able to predict the accurate duration of the initiation of the capsizing, where the motion is slow and the horizontal force is close to zero.

Various reasons suggest that this initial phase may not be relevant in the global context of the ultimate objective of the project, i.e. estimation of the volume loss on marine-terminating icebergs. To achieve this objective, we need to compare the modelled contact force with the inverted seismic source force. The very beginning of the seismic force has too small a signal-to-noise ratio, therefore it is the first peak of the force that is used as a reference to compare the seismic force and the modelled force. Also, because this force evolves very slowly at the beginning, it will not be responsible for the generation of seismic waves with a period of 50 s that is predominantly observed on glacial earthquake seismograms [Ekström Göran, 2003, Tsai and Ekström, 2007, Tsai et al., 2008, Sergeant et al., 2018]. Another reason for ignoring the beginning of the capsizing is that the duration of the initial slow rotation (phase i) of the iceberg is strongly dependent on the initial angle of inclination of the iceberg which is hard to constrain in the field data and has little effect on the capsizing (phases ii, iii, iv) when it is sufficiently small.

Nevertheless, if we consider a complete bedrock-glacier-iceberg-ocean system, the initial detachment of the iceberg can result in various other effects such as basal sliding or vertical oscillations of the glacier tongue, which can produce a seismic signal. Therefore the superposition of these phenomena can be erroneous if the timing is not well reproduced.

To solve this issue, simulations of the complete bedrock-glacier-iceberg-ocean system with a full fluid dynamics model coupled with a model for dynamics of deformable solids would seem to be unavoidable, however, as already discussed, it lies beyond actual computational possibilities.

## 5.3 Drag force and local pressure field

Following [Burton et al., 2012], a linear drag model with a local pressure proportional to the normal velocity  $|v_n|$  was also tested in SAFIM. It results in the following modification to equations (5) and (6):

$$\mathbf{F}_d = -\alpha \frac{1}{2} \int_{\Gamma_s} \rho_w |v_n| \text{sign}(v_n) \mathbf{n} d\Gamma, \quad (12)$$

$$\mathbf{M}_d = -\alpha \frac{1}{2} \int_{\Gamma_s} |v_n| \text{sign}(v_n) (\mathbf{r} - \mathbf{r}_G) \wedge \mathbf{n} d\Gamma. \quad (13)$$

Such a drag model yields poorer results than the original model with quadratic dependency when compared with the reference ISIS-CFD model. In addition, other drag models were tested with linear and quadratic pressure dependency on the velocity, with a non-uniform parameter  $\alpha$  on the surface of the iceberg and with drag depending on the sign of the local normal velocity  $v_n$ . Of all drag models tested, the most accurate was the model with quadratic dependency on the normal velocity and with a constant  $\alpha$ -factor over the whole surface of the iceberg. However, to better fit

the reference results, the  $\alpha$ -factor was made dependent on the iceberg's aspect ratio  $\varepsilon$ , which is an important difference with the original model presented in [Sergeant et al., 2018].

To further our understanding of the forces generated by the fluid, we analyse the hydrodynamic pressure distribution on the sides of the iceberg, computed by ISIS-CFD and defined as  $p_{dyn} = p_{tot} - p_{sta}$ , with  $p_{tot}$  the total fluid pressure and  $p_{sta}$  the hydrostatic pressure computed for the reference still water level ( $z = 0$ ). In particular, we attempted to establish a link between the spatial distribution of the hydrodynamic pressure on the iceberg and the local features of the fluid flow, notably with the normalized vorticity (see Fig. 5) which is defined as:  $\omega = -\sqrt{H/g} \mathbf{e}_y \cdot (\nabla \wedge \mathbf{u})$ , with a negative value (blue) accounting for a vortex rotating clockwise and a positive (red) value for a counter-clockwise vortex. On the four snapshots presented in Fig. 5, we also plot the dimensionless hydrodynamic pressure  $p'_{dyn} = p_{dyn}/(\rho_i H g)$ . The hydrodynamic pressure vectors are plotted in shaded pink and are shown with a dense array of vectors with the origin on the iceberg's surface and pointing outwards from the iceberg for a negative pressure and inwards for a positive pressure. Note that these values are about two orders of magnitude lower than the average hydrostatic pressure. The dynamic pressure is higher at locations where there is a vortex close to the surface of the iceberg such as on the corner furthest right in Figs. 5(b) and 5(c), on the bottom part of the left side and in the middle on the right side of the iceberg. This correlation suggests that the dynamic pressure field is highly dependent on the vortices in the fluid. Such an evolution of complex vortex motion cannot be reproduced within SAFIM and requires the resolution of the equations of fluid motion as in ISIS-CFD. Note that the high values of the pressure on the top side of the iceberg in Figs 5(c) and 5(d) are due to an additional hydrostatic pressure produced by the wave that is above the reference sea level.

We also attempted to correlate, in the full CFD simulations, the local hydrodynamic pressure  $p_{dyn}$  with the normal velocity  $v_n$  via a power law as is the case in SAFIM:

$$|p_{dyn}| = b|v_n|^a. \quad (14)$$

Note that in SAFIM, the coefficients are taken to be equal to  $a = 2$  and  $b = -\alpha \text{sign}(v_n) \rho_w/2$ . The coefficients  $a$  and  $b$  that minimize the error between  $p_{dyn}$  and  $b|v_n|^a$  (with a least square method on the log of equation 14) were calculated on portions of length  $W/2$  along the sides of the iceberg and at various times during the simulated capsize ( $\theta < 90^\circ$ ). We observed that the values of  $a$  and  $b$  vary along the sides of the iceberg and with time. Also, the accuracy of the fit varies along the sides: the accuracy is good on the bottom part of the long sides of the iceberg (least square coefficient  $R^2 > 0.9$ ) and poor on the top part of the long sides of the iceberg and close to the corners of the iceberg (least square coefficient  $R^2 < 0.5$ ). Also, we tried to correlate the dynamic pressure for  $a = 2$ , as in SAFIM, but there is no local correlation between the squared normal velocity and the dynamic pressure. Nevertheless, this choice ensures rather accurate overall drag forces and moments acting on the iceberg due to dynamic pressure.

## 5.4 Accuracy of added-mass values

The simplified added-masses, describing the diagonal terms of the added-mass matrix, will now be compared with the reference computed added-masses. Both added-mass matrices depend on the current configuration, more precisely on the  $z$ -coordinate of the centre of gravity  $G$  and on the tilt angle  $\theta$ , and therefore they should be updated at every time step. These matrices are calculated for the iceberg's kinetics computed by ISIS-CFD. We show the time evolution of the diagonal terms: horizontal added-mass  $m_{xx}$  in Fig. 11(a), the vertical added-mass  $m_{zz}$  in Fig. 11(b) and the added moment of inertia  $I_{\theta\theta}$  in Fig. 11(c), for the capsize of a laboratory-scale iceberg with  $\varepsilon = 0.246$  and  $H = 0.103\text{m}$ .

The simplified horizontal and vertical added-masses are in very good agreement with the corresponding computed added-masses: relative error (with the  $\mathcal{L}^2$  norm) of 21% on  $m_{xx}$  for  $\varepsilon = 0.246$  and 23% for  $\varepsilon = 0.496$ ; relative error of 11% on  $m_{zz}$  for  $\varepsilon = 0.246$  and 13% for  $\varepsilon = 0.496$ . The simplified added moment of inertia  $I_{\theta\theta}$  is assumed to be constant in our model whereas the computed added moment of inertia varies in time and has a smaller value: relative error (with the  $\mathcal{L}^2$  norm) of 48% for  $\varepsilon = 0.246$  and 52% for  $\varepsilon = 0.496$ .

For the aspect ratio  $\varepsilon = 0.246$ , the horizontal added-mass  $m_{xx}$  decreases from  $2.5\text{m}$  at the beginning down to  $\approx 0.23\text{m}$ , where  $m$  is the iceberg mass, whereas, symmetrically, the vertical added-mass  $m_{zz}$  increases from  $0.23\text{m}$  at the beginning up to  $\approx 2.5\text{m}$  at the end of the capsize. The horizontal added-mass  $m_{xx}$  measures the resistance of the fluid to a horizontal acceleration  $\ddot{x}_G$  of the iceberg. The iceberg has a longer submerged vertical extension (of the order of  $H$ ) at the beginning than at the end (of the order of  $W$ ) of the capsize, thus it needs to displace a

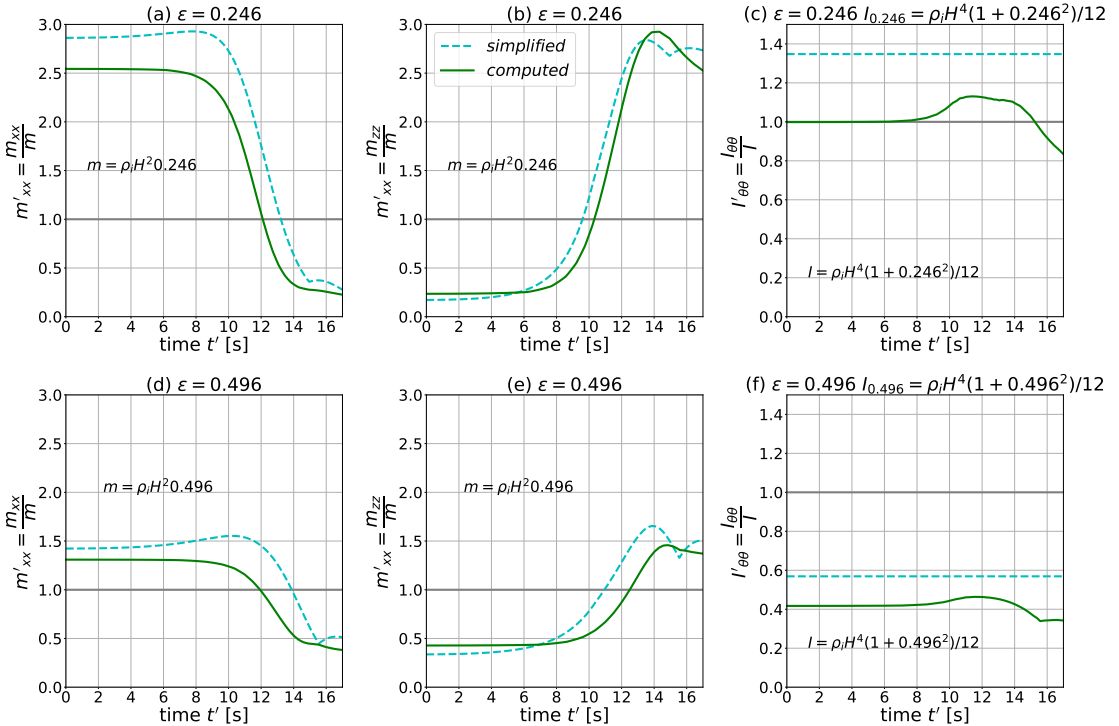


Figure 11: Time evolution of dimensionless horizontal added-masses (a) and (d), horizontal added-masses (b) and (e), added moment of inertia (c) and (f). The dashed cyan curves are the simplified added-masses and moment of inertia and the solid green curves are the computed added-masses and moment of inertia. Values are given for a laboratory-scale iceberg ( $H = 0.103$  m) with field densities and aspect ratio  $\varepsilon = 0.246$  in (a), (b) and (c) and  $\varepsilon = 0.496$  in (d), (e) and (f). For each aspect ratio  $\varepsilon$ , the values are normalized by the mass of the iceberg  $m = \rho_i H^2 \varepsilon$  and the inertia of the iceberg  $I = \rho_i H^4 (1 + \varepsilon^2)/12$ . The non-constant added-masses are given for the positions of the iceberg in the ISIS-CFD simulations. The values of the simplified added-masses are plotted for all coefficients equal to 1:  $C_x = C_z = C_\theta = 1$ .

greater volume of the fluid in a horizontal motion at the beginning than at the end of the capsizing ( $\theta > 90^\circ$ ). Therefore, a greater added-mass  $m_{xx}$  is expected at the beginning of the capsizing. The vertical added-masses  $m_{zz}$ , sensitive to the horizontal extension of the iceberg, experience the opposite variations in time. Also, the values of  $m_{xx}$  at the beginning of the capsizing are similar to those of  $m_{zz}$  at the end of the capsizing because they are closely linked to the iceberg length in the  $x$  and  $z$  directions as mentioned above. Similarly, the values of  $m_{xx}$  at the end of the capsizing are similar to those of  $m_{zz}$  at the beginning of the capsizing. For the aspect ratio  $\varepsilon = 0.246$ , the computed added moment of inertia is equal to the moment of inertia of the iceberg  $I$  at the beginning. Then it increases to  $1.25 I$  and decreases below the iceberg's moment of inertia to  $0.9 I$  (see Fig. 11).

For the aspect ratio  $\varepsilon = 0.496$ , the variations of the dimensionless added-masses are different:  $m_{xx}$  varies from  $1.3 \text{ m}$  to  $\approx 0.4 \text{ m}$  and  $m_{zz}$  varies from  $0.4 \text{ m}$  to  $\approx 1.4 \text{ m}$ . As for the  $\varepsilon = 0.246$  case, the value of  $m_{xx}$  at the beginning (resp. end) of the capsizing is close to that of  $m_{zz}$  at the end (resp. beginning) of the capsizing.

The added-masses (resp. inertia) are also of the same order of magnitude as the masses (resp. inertia) of the iceberg for other geometries. For the case of a two-dimensional thin ellipse with an aspect ratio of  $b/a$ , with  $a$  the along-flow dimension and  $b$  the cross-flow dimension, [Newman, 1999] gives the added-masses and added moment of inertia. For an ellipse with  $b/a = 0.2$ , the transverse added-mass is equal to 0.9 times the mass of the *displaced volume of fluid* (*i.e.* the submerged volume of the solid times the density of the fluid) and the added moment of inertia is equal to 0.7 times the inertia of the displaced volume of fluid. For similar densities for the fluid and the solid, the added-masses are close to 0.9 times the masses of the solid and the added moment of inertia is close to 0.7 times the inertia for the solid.

The optimized values of the coefficients for the added-masses in SAFIM (in terms of minimization of the error  $E_2$ , see Section 4.1) are:  $C_x = 0$ ,  $C_z = 0$  for all  $\varepsilon$ ,  $C_\theta = 0.75$  for  $\varepsilon = 0.246$  and  $C_\theta = 0.5$  for  $\varepsilon = 0.496$  (see Table 3). The optimized value  $C_z = 0$ , is consistent with the choice of  $m_{zz} = 0$  in [Tsai et al., 2008], however it is not equal to the computed vertical added-mass. The optimized coefficient  $C_x = 0$  gives  $m_{xx} = 0$ . The horizontal added-mass  $m_{xx}$  from [Tsai et al., 2008] varies similarly to the computed added-mass but is less accurate than the simplified added-mass with  $C_{xx} = 1$  and totally different from the optimized value  $m_{xx} = 0$ . The added moment of inertia  $I_{\theta\theta}$  with the formula in [Tsai et al., 2008] is constant throughout the capsizing and different from the optimized added moment of inertia. However, the formula for added-masses and added moment of inertia from [Tsai et al., 2008] were given for the simulation of an iceberg capsizing in contact with a wall, which may significantly affect the values of the added-masses. For  $\varepsilon = 0.246$ , note that the optimized simplified added moment of inertia ( $C_\theta = 0.75$ ) is close to the computed added moment of inertia. However, the simplified added moment of inertia is not in agreement with the computed added moment of inertia for higher  $\varepsilon$ . In other words, the values of the simplified added-mass matrix in SAFIM with the optimized parameters  $C_x$ ,  $C_z$  and  $C_\theta$  are not in agreement with the reference computed added-masses. However, as discussed in section 5.1, the SAFIM model with the simplified added-mass matrix gives better results than SAFIM with the computed added-mass matrix.

## 5.5 Effect of water/ice densities

The laboratory experiments were conducted with water and ice densities slightly different from those in the field (see Section 2.1). As shown in Fig. 12, the dynamics of the iceberg computed by ISIS-CFD with field densities is significantly different from those obtained with laboratory densities: the amplitude, duration and initiation of the capsizing are very sensitive to changes in densities. The results for both field and laboratory densities were obtained for the laboratory scale ( $H = 0.103 \text{ cm}$  and  $\varepsilon = 0.246$ ). This sensitivity is also well demonstrated by SAFIM with a drag model and without added-masses. Note that no change in the drag coefficient  $\alpha$  is needed to accurately reproduce this effect with SAFIM.

In Section 2.6, we pointed out the similarity between laboratory scale and field scale simulations if the same water and ice densities were used in both. To obtain the dimensionless variables, we used the time scale  $T_H = \sqrt{H/g}$ , length scale  $H$  and mass scale  $m$  (see Table 1). However, as shown in Fig. 12, using different densities yields great differences in the horizontal force. Here, we explain how a simulation of a laboratory-scale iceberg with laboratory densities can be related to a simulation of a field-scale iceberg with field densities. We use the same approach as in Section 2.6, with length scale  $H$  and mass scale  $m$ ; but we introduce a time scale depending on the densities

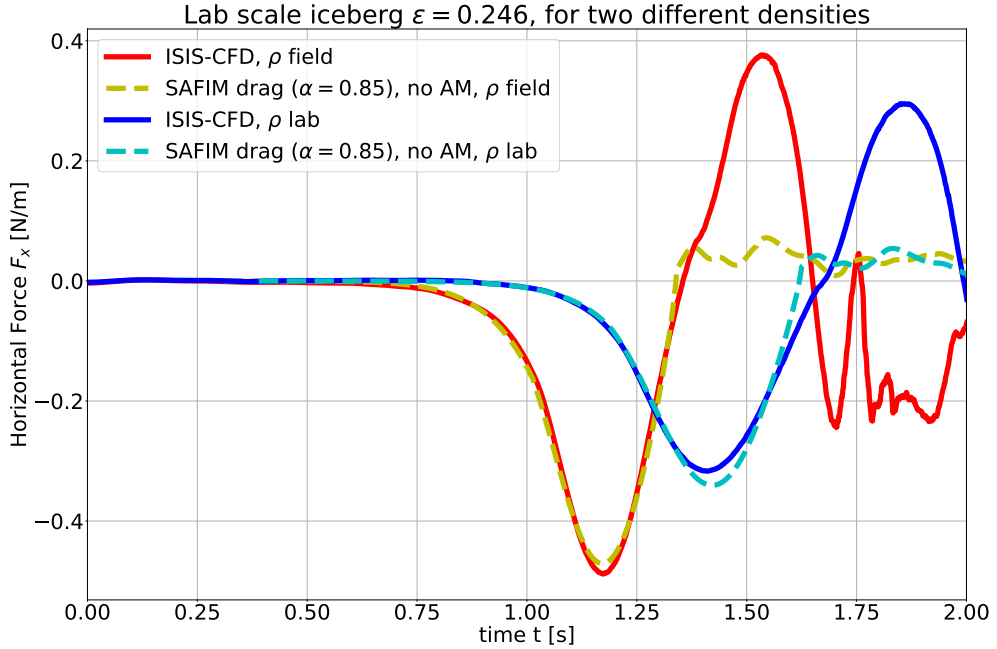


Figure 12: Horizontal force acting on a capsizing iceberg computed by ISIS-CFD and SAFIM for two different sets of densities: laboratory densities (red and yellow curves, "ρ lab" in the legend)  $\rho_w = 997 \text{ kg/m}^3$  and  $\rho_i = 920 \text{ kg/m}^3$  and field densities (blue and cyan curves, "ρ field" in the legend)  $\rho_w = 1025 \text{ kg/m}^3$  and  $\rho_i = 917 \text{ kg/m}^3$ . No change in the optimized parameter  $\alpha$  is needed to reproduce ISIS-CFD results by SAFIM.

as proposed by [Tsai et al., 2008] (ignoring the factor  $2\pi$ ):

$$T_{\rho,H} = \sqrt{\frac{H\rho_i}{g(\rho_w - \rho_i)}}.$$

In Fig. 13, we plot the dimensionless horizontal force  $F'_x = F_x T^2 / (mH)$  with respect to the dimensionless time  $t/T$  for time scale  $T = T_H$  (Figs 13 a, b, c) and for time scale  $T = T_{\rho,H}$  (Figs 13 d, e, f) and for three aspect ratios  $\varepsilon = 0.25$  (Figs 13 a, d),  $\varepsilon = 0.375$  (Figs 13 b, e) and  $\varepsilon = 0.5$  (Figs 13 c, f). For a time scale  $T_H$ , which does not involve densities, the dimensionless curves differ considerably whereas for  $T_{\rho,H}$ , which takes the densities into account, the agreement is largely improved, especially for small aspect ratios.

Using a shift in time, the fit can be improved even further. Therefore, to upscale the laboratory-scale experiments to the field scale, a dimensionless time scale  $T_{\rho,H}$  involving the difference in densities should be used rather than a simple scaling  $T_H$ . To attempt to reduce the remaining mismatch, a more elaborate time scale, length scale and mass scale - involving the initial angle of inclination or another formula dependent on the dimensions and densities - should be introduced.

The effect of the densities is taken into account in the time scale  $T_{\rho,H}$  through the square root of the ratio of the ice density divided by the water/ice density difference:

$$\text{for laboratory densities : } \sqrt{\rho_i/(\rho_w - \rho_i)} \Big|_{\text{lab}} \approx 3.46, \quad (15)$$

$$\text{for field densities : } \sqrt{\rho_i/(\rho_w - \rho_i)} \Big|_{\text{field}} \approx 2.92, \quad (16)$$

As densities seem to have a relatively large impact on capsize dynamics, more realistic water and ice densities, including their spatial heterogeneity, should probably be considered in future capsize models. Water density depends on salinity and temperature. For example, in the fjord of the Bowdoin glacier (northwest Greenland), water density may range between  $1015 \text{ kg/m}^3$  and  $1028 \text{ kg/m}^3$  [Ohashi et al., 2019, Sejr et al., 2017, Middelbo et al., 2018, Holding et al., 2019]. Ice density is more difficult to evaluate as in situ measurements are rare. It depends on the

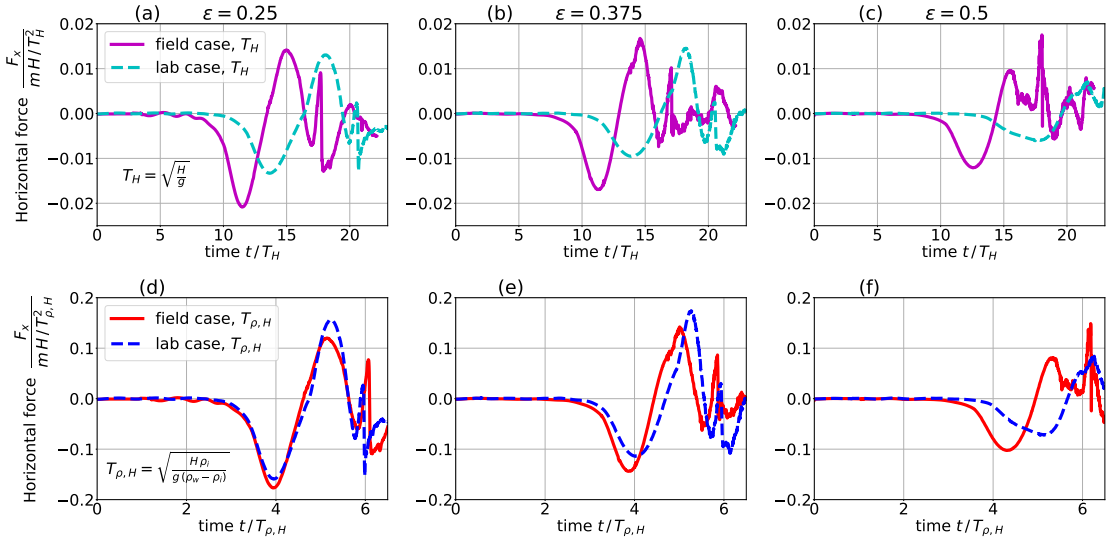


Figure 13: Dimensionless horizontal force acting on a capsizing iceberg computed by ISIS-CFD for a field-scale iceberg with field densities  $\rho_w = 1025 \text{ kg/m}^3$  and  $\rho_i = 917 \text{ kg/m}^3$  (solid lines) and for a laboratory-scale iceberg with laboratory densities  $\rho_w = 997 \text{ kg/m}^3$  and  $\rho_i = 920 \text{ kg/m}^3$  (dashed lines). The top row (a, b, c) is for time scale  $T_H = \sqrt{H/g}$  and the bottom row (d, e, f) is for time scale  $T_{\rho,H} = \sqrt{H/g} \sqrt{\rho_i/(\rho_w - \rho_i)}$ . The first (a, d), second (b, e) and third (c, f) columns correspond to  $\varepsilon = 0.25, 0.375$  and  $0.5$ , respectively.

volume fraction of air bubbles, which is for example around  $20 - 30\%$  for firn at  $\approx 40 \text{ m}$  in depth [Herron and Langway, 1980]. Ice density can also be increased if the iceberg contains melt pockets. The density of the iceberg may then be heterogeneous and can probably range between  $\approx 600 \text{ kg/m}^3$  and  $\approx 930 \text{ kg/m}^3$  (the density of pure ice at  $10^\circ\text{C}$  being  $918.7 \text{ kg/m}^3$ ).

With these ranges of ice and water field densities, the factor  $\sqrt{\rho_i/(\rho_w - \rho_i)}$  varies between the extreme values  $\approx 1.18$  and  $\approx 3.31$ , which corresponds to an even greater spread than in our lab/field comparison (equations 15 and 16). Therefore consideration of the effect of density and its variability has to be integrated in the inverse problem for iceberg volume estimation based on the seismic signal inversion.

## 5.6 3D effects

Capsizing icebergs have the following typical dimensions: full-glacier-height  $500 \text{ m} \lesssim H \lesssim 1000 \text{ m}$ , width in the glacier's flow direction  $W \lesssim 0.75H$  [MacAyeal and Scambos, 2003], width along the glacier's coast line, which is generally greater than the iceberg's height  $H \lesssim L$ , with an upper limit equal to the glacial fjord width. However, as discussed above, in our modelling we neglect the effect of the third dimension on the dynamics of the capsizing iceberg. The first argument to support this simplification is that iceberg capsizing in a narrow fjord-like tank (laboratory experiments of [Burton et al., 2012]) is very well reproduced with the two-dimensional ISIS-CFD model (Section 2). In the field, icebergs capsize in fjords with much more complex geometries. For example, the fjord may be much wider (in the  $e_y$  direction) than the iceberg which would yield a truly three-dimensional motion of the fluid. This motion of the fluid in the third direction can induce motion such as vortices on each side of the iceberg which may have an effect on the motion of the iceberg that has not yet been evaluated.

## 5.7 Effect of the iceberg geometry

This study was conducted with the assumption that the icebergs have a perfectly rectangular (parallelepipedic) shape and smooth surface. However, icebergs in the field have much more complex shapes. The freeboard of an iceberg has irregularities that can range from a scale larger than  $100 \text{ m}$  down to a scale less than  $0.1 \text{ m}$  [Landy et al., 2015]. The roughness of the submerged part of icebergs is poorly documented because of the difficulty in conducting suitable measurements. In future work, we could estimate the roughness of some well documented icebergs, such as the PII-B-1 tabular iceberg in Northwest Greenland scanned with a Reson 8125

multibeam sonar by [Wagner et al., 2014]. In fluid mechanics modelling, surface features have a great impact on the boundary layer close to the surface and in some cases also on the whole flow [Krogstad and Antonia, 1999]. A sensitivity analysis would be needed to assess the influence of the surface features and surface roughness on the dynamics of capsizing icebergs.

Furthermore, in our simulations, icebergs were initially in hydrostatic equilibrium. In [Sergeant et al., 2018], the effect of hydrostatic imbalance of the iceberg at the initiation of the capsize was assessed by varying the vertical position of the iceberg with respect to the water level. Hydrostatic imbalance results in a different evolution of the contact force and different dominant frequencies of generated seismic waves. This is supported by seismic observations of calving events.

## 6 Conclusion

In this study, we have improved the understanding of free iceberg capsize in open water through fluid-dynamics simulations (ISIS-CFD solver) validated against laboratory experiments [Burton et al., 2012]. In particular, we have shown the complexity of the fluid motion and the dynamics of the iceberg during capsize: vortices around the iceberg during and after capsize, motion of the fluid around the iceberg (velocity of  $\approx 88$  cm/s for a  $H = 800$  m high iceberg at a distance  $H$  from the iceberg), wave generation, iceberg submergence when reaching the horizontal position and a significant horizontal displacement of the iceberg during capsize. Moreover, we have shown that the non-dimensionalized horizontal force  $F'_x = F_x / (\rho_i H^2 \varepsilon g)$  is invariant with the height  $H$  of the iceberg.

We have presented here a Semi-Analytical Floating Iceberg Model (SAFIM) and demonstrated its accuracy for various geometries and water/ice densities by comparing the results with the direct numerical CFD simulations made by ISIS-CFD. Our simple model is slightly more complex but more accurate than the one used in our previous study [Sergeant et al., 2018]: the new feature is that the drag parameter depends on the iceberg aspect ratio (affine function) to minimize the error with the reference CFD simulations. SAFIM has an error of 5% to 20% on the horizontal force  $F_x$  (without added-masses) during the capsize phase for different geometries. An extension of this model to more complex iceberg shapes and to three dimensions is relatively straightforward.

Different options are offered by SAFIM. For accurate modelling of the amplitude of the fluid forces, SAFIM should be used with drag and without added-masses. For accurate modelling of the time of the peak force, it should be used with a drag force and an added moment of inertia. In the global context of estimations of iceberg volume by analysis of seismic signals generated during iceberg capsize in contact with a glacier front, based on the discussion on the time-shift Section 5.2, SAFIM should be used with an optimized drag coefficient  $\alpha$  and no added-masses. However, this model has been validated only for the case of capsize of an iceberg in the open ocean. Further validation should be conducted for the simulation of the capsize of an iceberg in contact with a glacier. In the geophysical context of modelling seismogenic iceberg capsize, further studies would help improve the model accuracy. Examples of such studies include (i) modelling of the full iceberg-ocean-glacier-bedrock system, which is computationally very challenging and (ii) sensitivity analysis of the iceberg dynamics to the iceberg shape, surface roughness and fjord geometry, which may be very complex.

## Acknowledgments

The authors acknowledge funding from ANR (contract ANR-11- BS01-0016 LANDQUAKES), ERC (contract ERC-CG-2013-PE10-617472 SLIDEQUAKES), DGA-MRIS and IPGP - Université de Paris ED560 (STEP'UP), which has made this work possible. The authors acknowledge Justin Burton for providing us data from laboratory experiments. The authors are also very grateful to Emmanuel de Langre (Department of Mechanics, LadHyX) for fruitful discussions. This is IPGP contribution number XXX.

## A Dimensional analysis and comparison of viscous and pressure forces

The Vashy-Buckingham -  $\pi$  theorem states that the problem can be written with  $n-p$  dimensionless ratios obtained by a combination of the  $n$  characteristic variables. The integer  $p$  is the number of independent physical dimensions in the iceberg capsize system, which is 3 (*time, length and mass*).

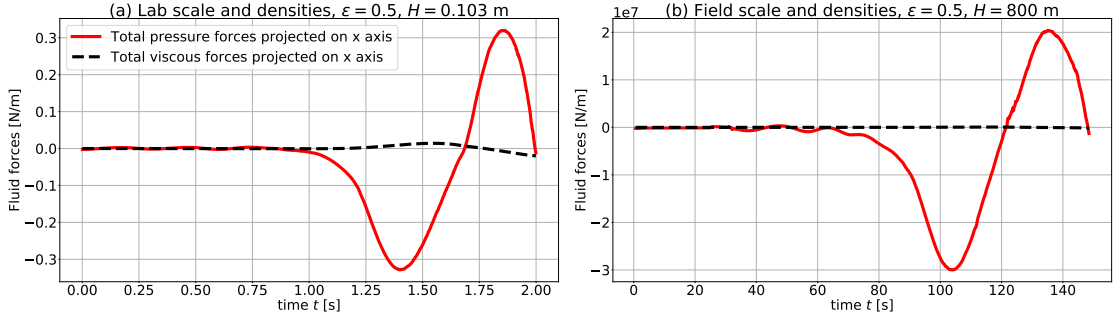


Figure 14: Viscous forces and pressure forces for (a) a laboratory-scale and (b) field-scale iceberg capsize, computed by ISIS-CFD.

The characteristic variables of the system are the dimensions,  $H$  and  $W$ , the densities  $\rho_i$  and  $\rho_w$ , the water viscosity  $\mu_w$  and gravity  $g$ , so  $n = 6$ .

The  $n - p = 3$  dimensionless ratios are chosen here to be:

$$\varepsilon, \frac{\rho_w}{\rho_i}, \frac{\mu_w}{\rho_w H^{3/2} g^{1/2}}$$

The calculation of the horizontal force  $F_x(t)$  from the  $n = 6$  independent characteristic variables of the problem can be written as:

$$F_x = f(H, W, \rho_i, \rho_w, \mu_w, g)$$

The Vashy-Buckingham -  $\pi$  theorem states that the problem can be written:

$$\frac{F_x}{mg} = \mathcal{G}(\varepsilon, \frac{\rho_w}{\rho_i}, \frac{\mu_w}{\rho_w H^{3/2} g^{1/2}}) \quad (17)$$

To estimate the effect of viscosity, we compare the pressure and viscous forces. The fluid force on the surface of the iceberg calculated by ISIS-CFD is the sum of a friction-induced force (locally tangent to the fluid/solid interface) and a pressure-induced force (normal to this interface). In the case of an iceberg with aspect ratio  $\varepsilon = 0.25$ , the friction force is found to be  $\approx 300$  times smaller than the pressure force for the field-scale case ( $H = 800$  m) and  $\approx 10$  times smaller for the laboratory case ( $H = 0.103$  m) as illustrated in Fig. 14. Therefore, viscous effects can be reasonably neglected in both scales. This leads to the following approximation for equations (17):

$$\frac{F_x}{mg} \approx \mathcal{G}(\varepsilon, \frac{\rho_w}{\rho_i}), \quad (18)$$

i.e. for similar initial conditions and boundary conditions, the evolution with time of the dimensionless force  $F'_x = \frac{F_x}{mg}$  only depends on the aspect ratio  $\varepsilon$  and the density ratio  $\frac{\rho_w}{\rho_i}$ . However, the function  $f$  remains unknown and is investigated in Section 2.6 and Section 5.5.

## B Integrated expressions of SAFIM hydrostatic force, drag force, torque and simplified added-masses

### B.1 Integrated expressions of SAFIM hydrostatic and drag forces and torque

The integrated expressions for hydrostatic and drag forces and the associated moments are given below for SAFIM and for a rectangular iceberg as in Fig. 1. All these expressions are implemented in the Python code available online at [\[Yastrebov and Bonnet, 2020\]](#).

The effect of the hydrostatic pressure is given by the following integral:  $\mathbf{F}_s = -\rho_w g \int_{\Gamma_s} z \mathbf{n} d\Gamma$ , where  $\mathbf{n}$  is the outward surface normal and  $\Gamma_s$  is the submerged part of the iceberg. The torque induced by this pressure distribution with respect to the centre of gravity  $G$  at position  $\mathbf{r}_G$  is given by:  $\mathbf{M}_s = -\rho_w g \int_{\Gamma_s} (\mathbf{r} - \mathbf{r}_G) \wedge \mathbf{n} d\Gamma$

The drag force is:

$$\mathbf{F}_d = \frac{1}{2} \alpha \rho_w \int_{\Gamma_s} |v_n|^2 \text{sign}(v_n) \mathbf{n} d\Gamma, \quad (19)$$

where  $v_n$  is the local normal velocity component. The drag moment with respect to  $G$  is:

$$\mathbf{M}_d = \frac{1}{2} \alpha \rho_w \int_{\Gamma_s} |v_n|^2 \text{sign}(v_n) (\mathbf{r} - \mathbf{r}_G) \wedge \mathbf{n} d\Gamma \quad (20)$$

The calculation of the integral of the pressure drag is split into integration over all submerged or partly submerged sides of the rectangular iceberg. Consider a partly submerged side  $S = AB$  and let us assume that corner  $A$  is a submerged corner and  $B$  is a corner outside the water. Then the velocity  $\mathbf{v}_M$  of a point  $M \in [AB]$  is:

$$\mathbf{v}_M = \dot{\mathbf{r}}_G + \dot{\theta} \mathbf{e}_y \wedge (\mathbf{r}_M - \mathbf{r}_G), \quad (21)$$

where  $\mathbf{r}_M = \mathbf{r}_A + \xi(\mathbf{r}_B - \mathbf{r}_A)$  with  $\xi \in [0, \xi_i]$  and  $\xi_i$  defining the position of the point on the given side located at the sea level. So for the side  $AB$ , the contribution of the drag force is given by

$$F_d^{AB} = \frac{1}{2} \alpha \rho_w \mathbf{n} \|\mathbf{r}_B - \mathbf{r}_A\| \int_0^{\xi_i} |v_n|^2 \text{sign}(v_n) d\xi,$$

where

$$v_n = \dot{\mathbf{r}}_G \cdot \mathbf{n} + \dot{\theta} \mathbf{e}_y \wedge (\mathbf{r}_A + \xi(\mathbf{r}_B - \mathbf{r}_A) - \mathbf{r}_G) \cdot \mathbf{n}.$$

For the case of a totally submerged side then  $\xi_i = 1$ . For the case of a side totally outside the water, the contribution to the drag force is zero.

## B.2 Qualitative explanation of horizontal motion of the capsizing iceberg

With the formulation of the drag force given above, we can reproduce the horizontal motion of a freely capsizing iceberg, which is observed experimentally and reproduced with the accurate ISIS-CFD simulations. Obtaining a closed form solution of SAFIM equations Eqs. (1), (2) and (3) is out of reach. We wish to give here some intuitive explanation of the horizontal motion of the iceberg. The resultant of the buoyancy and gravity forces moves the iceberg upwards and makes it rotate: these two effects initiate the vertical and rotational motion of the iceberg. The induced velocity produces a force with a non-zero horizontal component.

We now explain why these two initial motions -upwards and rotation-, together generate a horizontal drag force, in the framework of SAFIM. We draw the velocity  $\mathbf{v}$  (triple red arrow) of several points on the surface of the iceberg and its normal component  $v_n \mathbf{n}$  (dashed red arrow). In SAFIM, the elementary drag force  $d\mathbf{F}_d$  (solid black arrow) is collinear with  $\mathbf{n}$  and opposes the normal velocity  $v_n \mathbf{n}$ . The projection of the elementary drag forces on the horizontal axis  $d\mathbf{F}_{d_x} = (d\mathbf{F}_d \cdot \mathbf{e}_x) \mathbf{e}_x$  is shown by a dashed green arrow if it is leftward and dashed blue arrow if it is rightward. The integral of these horizontal elemental forces results in the global horizontal force  $\mathbf{F}_d \cdot \mathbf{e}_x$ . For the case of upward motion Fig. 15(a) of the iceberg (Fig. 15(a)), the vertical local velocity is constant along the iceberg surface. First, we show that the contribution to the horizontal drag force of all the points on the two long sides of the iceberg is a leftward elementary force  $d\mathbf{F}_{d_x}$ . As shown in Fig. 15, on both long sides on the iceberg, the projection of the velocity on the normal vectors  $v_n \mathbf{n}$  is rightward and the opposite vector, which gives the direction of  $d\mathbf{F}_d$ , has a negative horizontal component, i.e.  $d\mathbf{F}_{d_x}$  is a leftward force. Second, on the small submerged side  $CD$ , the horizontal elementary force  $d\mathbf{F}_{d_x}$  is rightward but with a smaller amplitude than on the long side because of the different inclination of that side compared to the long sides. This is valid as long as the iceberg has an aspect ratio smaller than 1 and is tilted less than  $\theta = 45^\circ$ . This is the case here since we assess the initialization of the horizontal motion for a small initial inclination of the iceberg ( $\theta_i \leq 15$  in the simulations) and for unstable icebergs, i.e. icebergs with aspect ratios  $\varepsilon < \varepsilon_c < 1$  (see Section 2.1). Additionally, the surface of the iceberg contributing to a leftward drag force (in green) is longer and has larger elementary horizontal forces than the surface of the iceberg contributing to a rightward force (in dark blue). Therefore, the horizontal force resulting from the upward motion is leftward. For the case of rotational motion (Fig. 15(b)), the velocity increases with the distance to the centre of rotation. Because we assume no initial

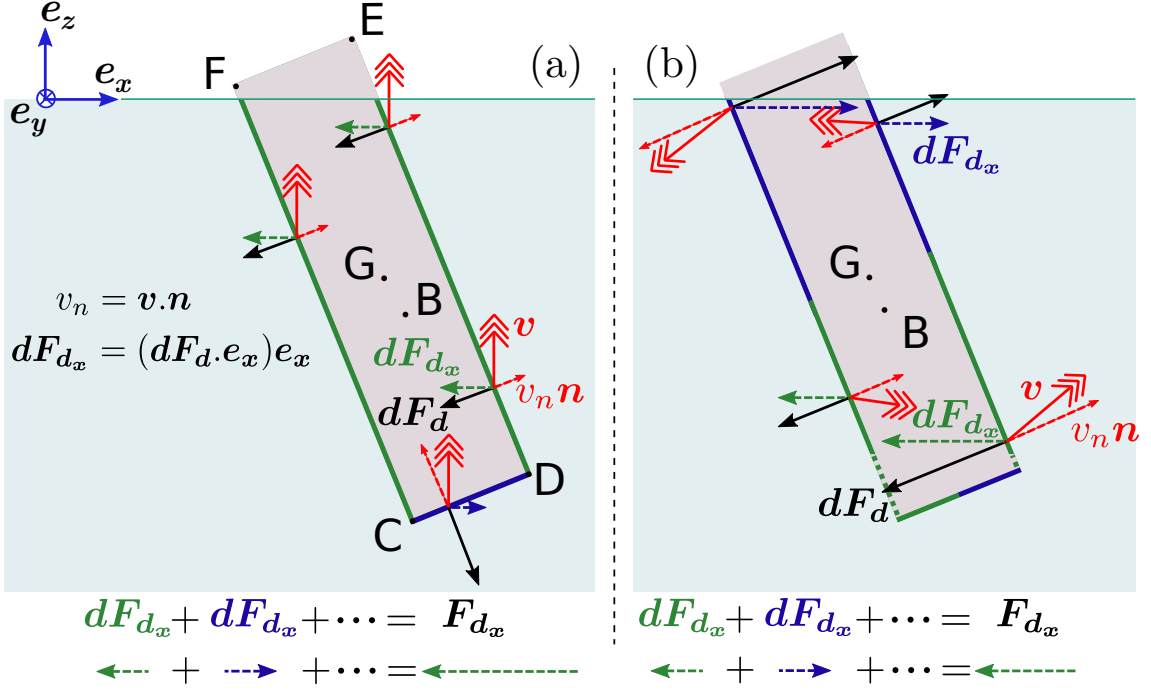


Figure 15: Schematic explanation of the horizontal force induced by the formulation of the drag force in SAFIM (a) vertical upward motion of iceberg, (b) rotation of iceberg.

horizontal motion of the iceberg,  $G$  is initially immobile and the iceberg rotates around  $G$ . The further away the point is, the more it contributes to the drag force. Two points located at the same distance from  $G$ , but with opposite normal velocity vectors  $v_n \mathbf{n}$  (i.e. one point on the blue line and one point on the green line) have the same absolute contribution to the drag force but in opposite directions. Thus the drag force on the part of the surface coloured solid green compensates the drag force on the part coloured blue. The remaining part of the surface illustrated by dashed green lines, induces a leftward total horizontal force. Therefore, by superposing vertical and rotation motion, we obtain a net drag force in the direction of the initial tilt of the iceberg's top, here to the left.

### B.3 Integrated expressions of simplified added-masses

The calculation of the simplified added-masses given in equation (7), requires the calculation of the effective height  $H_{\text{eff}}$  and effective width  $W_{\text{eff}}$  of the submarine part of the iceberg (see Fig. 1). To calculate them, we use the positions of the four corners:  $C, D, E, F$  (Fig. 15). The coordinates of a corner  $P \in \{C, D, E, F\}$  have the general expression :

$$x_P = z_G + \delta_1^P \frac{H}{2} \cos(\theta) + \delta_2^P \frac{L}{2} \sin(\theta)$$

$$z_P = z_G + \delta_3^P \frac{H}{2} \cos(\theta) + \delta_4^P \frac{L}{2} \sin(\theta)$$

with  $(\delta_1^P, \delta_2^P, \delta_3^P, \delta_4^P)$  defined as follows for the four corners

$$\{\delta_1^C, \delta_2^C, \delta_3^C, \delta_4^C\} = \{1, -1, -1, -1\}, \quad \{\delta_1^D, \delta_2^D, \delta_3^D, \delta_4^D\} = \{1, 1, -1, 1\},$$

$$\{\delta_1^E, \delta_2^E, \delta_3^E, \delta_4^E\} = \{-1, 1, 1, -1\}, \quad \{\delta_1^F, \delta_2^F, \delta_3^F, \delta_4^F\} = \{-1, -1, 1, 1\}.$$

The effective height can be calculated with the following expressions :

$$H_{\text{eff}} = \max((z_w - z_C); (z_w - z_D); (z_w - z_E); (z_w - z_F))$$

where  $z_w$  is the water level.

The effective width, defined as the distance between the leftmost and the rightmost points of the submerged part of the iceberg, is calculated similarly, but after checking which are the submerged corners and the geometrical intersection between the water surface and the iceberg sides.

$\epsilon$	$\theta_0$ [°]	no AM		computed AM		simplified AM				
		Error $E_1$	$\alpha$	Error $E_2$	$\alpha$	Error $E_2$	$\alpha$	$C_x$	$C_z$	$C_I$
0.246	0.5	5.2%	0.85	36.6%	3	10.0%	1.1	0.	0.	0.75
0.374	0.5	9.6%	1.55	34.1%	1.8	21.3%	1.4	0.	0.	0.75
0.496	0.5	20.1%	2.9	40.0%	1.9	23.0%	3.0	0.	0.	0.5
0.639	15	24.7%	4.0	47.4%	2.6	26.2%	4.2	0.	0.	0.25

Table 3: First two columns : geometrical characteristics and initial conditions of the studied icebergs. Laboratory-scale iceberg simulations have height  $H = 0.1$  m and field-scale iceberg simulations have height  $H = 800$  m. The density of the water is  $\rho_w = 1025$  kg m<sup>-3</sup> and the density of the ice is  $\rho_i = 917$  kg m<sup>-3</sup>. Next columns : parameters minimizing the error on  $F_x$  and the corresponding error for SAFIM without added-masses, SAFIM with computed added-masses and SAFIM with simplified added-masses.

## C Errors and values of the parameters for SAFIM

We summarize in Table 3 the errors of SAFIM computed with respect to the ISIS-CFD results for a quadratic drag model and the three options for added-masses (no added-masses, simplified or computed added-masses). These errors correspond to the minimal possible errors obtained by the minimization procedure. The step used for the drag coefficient  $\alpha$  was 0.05 and the step for the added-masses factors was 0.25.

## References

[Amundson et al., 2012] Amundson, J. M., Burton, J. C., and Correa-Legisos, S. (2012). Impact of hydrodynamics on seismic signals generated by iceberg collisions. *Annals of Glaciology*, 53(60):106–112.

[Amundson et al., 2010] Amundson, J. M., Fahnestock, M., Truffer, M., Brown, J., Lüthi, M. P., and Motyka, R. J. (2010). Ice mélange dynamics and implications for terminus stability, Jakobshavn Isbræ, Greenland. *Journal of Geophysical Research: Earth Surface*, 115(1).

[Benn et al., 2017] Benn, D. I., Cowton, T., Todd, J., and Luckman, A. (2017). Glacier Calving in Greenland. *Current Climate Change Reports*, 3(4):282–290.

[Burton et al., 2012] Burton, J. C., Amundson, J. M., Abbot, D. S., Boghosian, A., Cathles, L. M., Correa-Legisos, S., Darnell, K. N., Guttenberg, N., Holland, D. M., and MacAyeal, D. R. (2012). Laboratory investigations of iceberg capsizing dynamics, energy dissipation and tsunamigenesis. *Journal of Geophysical Research: Earth Surface*, 117(1):1–13.

[Burton et al., 2013] Burton, J. C., Cathles, L. M., and Wilder, W. G. (2013). The role of cooperative iceberg capsizing in ice-shelf disintegration. *Annals of Glaciology*, 54(63):84–90.

[Cassotto et al., 2019] Cassotto, R., Fahnestock, M., Amundson, J. M., Truffer, M., Boettcher, M. S., De La Peña, S., and Howat, I. (2019). Non-linear glacier response to calving events, Jakobshavn Isbræ, Greenland. *Journal of Glaciology*, 65(249):39–54.

[Durand et al., 2014] Durand, M., Leroyer, A., Lothodé, C., Hauville, F., Visonneau, M., Floch, R., and Guillaume, L. (2014). FSI investigation on stability of downwind sails with an automatic dynamic trimming. *Ocean Engineering*, 90(2013):129–139.

[Ekström Göran, 2003] Ekström Göran, Nettles M., A. A. G. (2003). Glacial Earthquakes. *Science*, 622(2003):10–13.

[Enderlin et al., 2014] Enderlin, E. M., Howat, I. M., Jeong, S., Noh, M.-J., van Angelen, J. H., and van den Broeke, M. R. (2014). An improved mass budget for the Greenland ice sheet. *Geophysical Prospecting*, 41(9):3307–3314.

[Guilmeneau et al., 2017] Guilmeneau, E., Deng, G. B., Leroyer, A., Queutey, P., Visonneau, M., and Wackers, J. (2017). Numerical simulations for the wake prediction of a marine propeller in straight-ahead flow and oblique flow. *Journal of Fluids Engineering, Transactions of the ASME*, 140(2).

[Guilmineau et al., 2018] Guilmineau, E., Deng, G. B., Leroyer, A., Queutey, P., Visonneau, M., and Wackers, J. (2018). Wake prediction of a marine propeller: The role of the turbulence closures. *ERCOFTAC Series*, 24:251–256.

[Hay et al., 2006] Hay, A., Leroyer, A., and Visonneau, M. (2006). H-adaptive Navier-Stokes simulations of free-surface flows around moving bodies. *Journal of Marine Science and Technology*, 11(1):1–18.

[Herron and Langway, 1980] Herron, M. M. and Langway, C. C. (1980). Firn densification: an empirical model. 25(93):373–385.

[Holding et al., 2019] Holding, J. M., Markager, S., Juul-Pedersen, T., Paulsen, M. L., Møller, E. F., Meire, L., and Sejr, M. K. (2019). Seasonal and spatial patterns of primary production in a high-latitude fjord affected by Greenland Ice Sheet run-off. *Biogeosciences*, 16(19):3777–3792.

[Jay Zwally et al., 2011] Jay Zwally, H., Li, J., Brenner, A. C., Beckley, M., Cornejo, H. G., Marzio, J. D., Giovinetto, M. B., Neumann, T. A., Robbins, J., Saba, J. L., Yi, D., and Wang, W. (2011). Greenland ice sheet mass balance: Distribution of increased mass loss with climate warming; 2003-07 versus 1992-2002. *Journal of Glaciology*, 57(201):88–102.

[Job, 1978] Job, J. (1978). Numerical Modelling of Iceberg Towing for Water Supplies, A Case Study. *Journal of Glaciology*, 20(84):533–542.

[Krogstad and Antonia, 1999] Krogstad, P. Å. and Antonia, R. A. (1999). Surface roughness effects in turbulent boundary layers. *Experiments in Fluids*, 27(5):450–460.

[Landy et al., 2015] Landy, J. C., Isleifson, D., Komarov, A. S., and Barber, D. G. (2015). Parameterization of centimeter-scale sea ice surface roughness using terrestrial LiDAR. *IEEE Transactions on Geoscience and Remote Sensing*, 53(3):1271–1286.

[Lemke et al., 2007] Lemke, P., Ren, J., Alley, R., Allison, I., Carrasco, J., Flato, G., Fujii, Y., Kaser, G., Mote, P., Thomas, R., et al. (2007). Observations: changes in snow, ice and frozen ground, climate change 2007: The physical science basis. contribution of working group i to the fourth assessment report of the intergovernmental panel on climate change. *Cambridge University Press*. UK, Cambridge, pages 337–383.

[Leroyer et al., 2012] Leroyer, A., Barré, S., and J.-M., K. (2012). Experiments and simulations: approach and steps towards a better knowledge of the hydrodynamics of rowing blades. *Movement et Sport Sciences*, 75(2012/1 (n 75)):85–96.

[Leroyer and Visonneau, 2005] Leroyer, A. and Visonneau, M. (2005). Numerical methods for RANSE simulations of a self-propelled fish-like body. *Journal of Fluids and Structures*, 20(7):975–991.

[Leroyer et al., 2011] Leroyer, A., Wackers, J., Queutey, P., and Guilmineau, E. (2011). Numerical strategies to speed up CFD computations with free surface - Application to the dynamic equilibrium of hulls. *Ocean Engineering*, 38(17-18):2070–2076.

[MacAyeal and Scambos, 2003] MacAyeal, D. R. and Scambos, T. A. (2003). Catastrophic ice-shelf break-up by an ice-shelf-fragment-capsize mechanism. *Journal of Glaciology*, 49.

[Marsh et al., 2015] Marsh, R., Ivchenko, V. O., Skliris, N., Alderson, S., Bigg, G. R., Madec, G., Blaker, A. T., Aksenov, Y., Sinha, B., Coward, A. C., Le Sommer, J., Merino, N., and Zalesny, V. B. (2015). NEMO-ICB (v1.0): Interactive icebergs in the NEMO ocean model globally configured at eddy-permitting resolution. *Geoscientific Model Development*, 8(5):1547–1562.

[Menter, 1993] Menter, F. (1993). Zonal two equation kw turbulence models for aerodynamic flows. In *23rd fluid dynamics, plasmadynamics, and lasers conference*, page 2906.

[Middelbo et al., 2018] Middelbo, A. B., Sejr, M. K., Arendt, K. E., and Møller, E. F. (2018). Impact of glacial meltwater on spatiotemporal distribution of copepods and their grazing impact in Young Sound NE, Greenland. *Limnology and Oceanography*, 63(1):322–336.

[Mizine et al., 2009] Mizine, I., Karafiath, G., Queutey, P., and Visonneau, M. (2009). Interference Phenomenon in Design of Trimaran Ship. *10th International Conference on Fast Sea Transportation FAST 2009*, Athens, Greece, October 2009, FAST 2009(October).

[Molin, 2002] Molin, B. (2002). Hydrodynamique des structures offshore. Technip.

[Moon et al., 2016] Moon, T., Heide-Jørgensen, M. P., Dietz, R., Laidre, K. L., Hudson, B., McGovern, R., and Hauser, D. D. W. (2016). Use of glacial fronts by narwhals ( *Monodon monoceros* ) in West Greenland . Biology Letters, 12(10):20160457.

[Morison et al., 1950] Morison, J., Johnson, J., and Schaaf, S. (1950). The Force Exerted by Surface Waves on Piles. Journal of Petroleum Technology, 2(05):149–154.

[Murray et al., 2015] Murray, T., Nettles, M., Selmes, N., Cathles, L. M., Burton, J. C., James, T. D., Edwards, S., Martin, I., O’Farrell, T., Aspey, R., Rutt, I., and Baugé, T. (2015). Reverse glacier motion during iceberg calving and the cause of glacial earthquakes. Science, 349(6245):305–308.

[Newman, 1999] Newman, J. N. (1999). Marine Hydrodynamics-The MIT Press. The MIT Press.

[Ohashi et al., 2019] Ohashi, Y., Aoki, S., Matsumura, Y., Sugiyama, S., Kanna, N., and Sakakibara, D. (2019). Water mass structure and the effect of subglacial discharge in Bowdoin Fjord, northwestern Greenland. Ocean Science Discussions, xxx(May):1–30.

[Peters et al., 2014] Peters, I., Cassotto, R., Amundson, J. M., Fahnestock, M., and Darnell, K. (2014). Dynamic jamming of iceberg-choked fjords. Geophysical Research Letters, 42:1–8.

[Queutey and Visonneau, 2007] Queutey, P. and Visonneau, M. (2007). An interface capturing method for free-surface hydrodynamic flows. Computers and Fluids, 36(9):1481–1510.

[Queutey et al., 2014] Queutey, P., Wackers, J., Leroyer, A., Deng, G., Guilmeneau, E., Visonneau, M., Hagesteijn, G., and Brouwer, J. (2014). Dynamic Behaviour of the Loads of Podded Propellers in Waves: Experimental and Numerical Simulations. In Volume 8A: Ocean Engineering.

[Robert et al., 2019] Robert, Y., Leroyer, A., Barré, S., Queutey, P., and Visonneau, M. (2019). Validation of cfd simulations of the flow around a full-scale rowing blade with realistic kinematics. Journal of Marine Science and Technology, 24(4):1105–1118.

[Savage, 2007] Savage, S. (2007). Aspects of Iceberg Deterioration and Drift. Geomorphological Fluid Mechanics, pages 279–318.

[Sejr et al., 2017] Sejr, M. K., Stedmon, C. A., Bendtsen, J., Abermann, J., Juul-Pedersen, T., Mortensen, J., and Rysgaard, S. (2017). Evidence of local and regional freshening of Northeast Greenland coastal waters /704/106/829/2737 /704/829/2737 article. Scientific Reports, 7(1).

[Sergeant et al., 2016] Sergeant, A., Mangeney, A., Stutzmann, E., Montagner, J. P., Walter, F., Moretti, L., and Castelnau, O. (2016). Complex force history of a calving-generated glacial earthquake derived from broadband seismic inversion. Geophysical Research Letters, 43(3):1055–1065.

[Sergeant et al., 2019] Sergeant, A., Mangeney, A., Yastrebov, V. A., Walter, F., Montagner, J.-p., Castelnau, O., Bonnet, P., Ralaiarisoa, V. J.-l., Bevan, S., and Luckman, A. (2019). Monitoring Greenland ice-sheet buoyancy-driven calving discharge using glacial earthquakes. Annals of Glaciology, 60(000):75–95.

[Sergeant et al., 2018] Sergeant, A., Yastrebov, V., Mangeney, A., Castelnau, O., Montagner, J., and Stutzmann, E. é. o. (2018). Numerical Modeling of Iceberg Capsizing Responsible for Glacial Earthquakes. Journal of Geophysical Research: Earth Surface, 123(11):3013–3033.

[Spalart and Allmaras, 1992] Spalart, P. R. and Allmaras, S. R. (1992). A one-equation turbulence model for aerodynamic flows. 30th Aerospace Sciences Meeting and Exhibit, 112(3):1–13.

[Todd and Christoffersen, 2014] Todd, J. and Christoffersen, P. (2014). Are seasonal calving dynamics forced by buttressing from ice mélange or undercutting by melting? Outcomes from full-Stokes simulations of Store Glacier, West Greenland. Cryosphere, 8(6):2353–2365.

[Tsai and Ekström, 2007] Tsai, V. C. and Ekström, G. (2007). Analysis of glacial earthquakes. Journal of Geophysical Research: Earth Surface, 112(3):1–13.

[Tsai et al., 2008] Tsai, V. C., Rice, J. R., and Fahnestock, M. (2008). Possible mechanisms for glacial earthquakes. Journal of Geophysical Research: Earth Surface, 113(3):1–17.

[Tsukrov et al., 2002] Tsukrov, I., Eroshkin, O., Fredriksson, D., Swift, M. R., and Celikkol, B. (2002). Finite element modeling of net panels using a consistent net element. *Ocean Engineering*, 30(2):251–270.

[van den Broeke et al., 2009] van den Broeke, M., Bamber, J., Ettema, J., Rignot, E., Schrama, E., van De Berg, W. J., van Meijgaard, E., Velicogna, I., and Wouters, B. (2009). Partitioning recent Greenland mass loss. Supporting online material. *Science (New York, N.Y.)*, 326(5955):984–6.

[Van Den Broeke et al., 2016] Van Den Broeke, M. R., Enderlin, E. M., Howat, I. M., Kuipers Munneke, P., Noël, B. P., Jan Van De Berg, W., Van Meijgaard, E., and Wouters, B. (2016). On the recent contribution of the Greenland ice sheet to sea level change. *Cryosphere*, 10(5):1933–1946.

[Venugopal et al., 2009] Venugopal, V., Varyani, K., and Westlake, P. (2009). Drag and inertia coefficients for horizontally submerged rectangular cylinders in waves and currents. *Proceedings of the Institution of Mechanical Engineers, Part M: Journal of Engineering for the Maritime Environment*, 223(1):121–136.

[Visonneau, 2005] Visonneau, M. (2005). A step towards the numerical simulation of viscous flows around ships at full scale - recent achievements within the European Union Project Effort. Technical report, Ecole Centrale de Nantes.

[Visonneau et al., 2016] Visonneau, M., Deng, G. B., Guilmineau, E., Queutey, P., and Wackers, J. (2016). Local and Global Assessment of the Flow around the Japan Bulk Carrier with and without Energy Saving Devices at Model and Full Scale. Technical report, Ecole Centrale de Nantes.

[Visonneau et al., 2006] Visonneau, M., Queutey, P., and Deng, G. (2006). Model and full-scale free-surface viscous flows around fully-appended ships.

[Vizcaino et al., 2015] Vizcaino, M., Enderlin, E. M., van den Broeke, M. R., Lenaerts, J. T. M., Le Bars, D., and van Kampenhout, L. (2015). Representing Greenland ice sheet freshwater fluxes in climate models. *Geophysical Research Letters*, 42(15):6373–6381.

[Wackers et al., 2012] Wackers, J., Deng, G., Leroyer, A., Queutey, P., and Visonneau, M. (2012). Adaptive grid refinement for hydrodynamic flows. *Computers and Fluids*.

[Wagner et al., 2017] Wagner, T. J., Stern, A. A., Dell, R. W., and Eisenman, I. (2017). On the representation of capsizing in iceberg models. *Ocean Modelling*, 117:88–96.

[Wagner et al., 2014] Wagner, T. J., Wadhams, P., Bates, R., Elosegui, P., Stern, A., Vella, D., Abrahamsen, E. P., Crawford, A., and Nicholls, K. W. (2014). The "footloose" mechanism: Iceberg decay from hydrostatic stresses. *Geophysical Research Letters*, 41(15):5522–5529.

[Walter et al., 2012] Walter, F., Amundson, J. M., O'Neil, S., Truffer, M., Fahnestock, M., and Fricker, H. A. (2012). Analysis of low-frequency seismic signals generated during a multiple-iceberg calving event at Jakobshavn Isbr, Greenland. *Journal of Geophysical Research: Earth Surface*, 117(1):1–11.

[Wendel, 1956] Wendel, K. (1956). *Hydrodynamic Masses and Hydrodynamic Moments of Inertia*. PhD thesis, Hamburg. Translated in English by E.N. Labouvie and A. Borden. Available online at <http://hdl.handle.net/1721.3/51294>.

[Yastrebov and Bonnet, 2020] Yastrebov, V. A. and Bonnet, P. (2020). SAFIM: Semi-Analytical Floating Iceberg Model. Available online, DOI:10.5281/zenodo.3783774.

[Yvin et al., 2018] Yvin, C., Leroyer, A., Visonneau, M., and Queutey, P. (2018). Added mass evaluation with a finite-volume solver for applications in fluid–structure interaction problems solved with co-simulation. *Journal of Fluids and Structures*, 81:528–546.